

A landslide runout model for sediment transport, landscape evolution and hazard assessment applications

Jeffrey Keck^{1,2}, Erkan Istanbuluoglu¹, Benjamin Campforts³, Gregory Tucker^{4,5}, Alexander Horner-Devine¹

¹ University of Washington, Civil and Environmental Engineering, Seattle, WA, USA

² Washington Department of Natural Resources, Forest Resources Division, Olympia, WA, USA

³ Department of Earth Sciences, Vrije University, Amsterdam, Netherlands

⁴ Department of Geological Sciences, University of Colorado Boulder, Boulder, CO, USA

⁵ Cooperative Institute for Research in Environmental Sciences (CIRES), University of Colorado Boulder, Boulder, CO, USA

Correspondence to: Jeffrey Keck (keckje@gmail.com)

Abstract

We developed a new rule-based, cellular-automaton algorithm for predicting the hazard extent, sediment transport and topographic change associated with the runout of a landslide. This algorithm, which we call MassWastingRunout (MWR), is coded in Python and implemented as a component for the package Landlab. MWR combines the functionality of simple runout algorithms used in landscape evolution and watershed sediment yield models with the predictive details typical of runout models used for landslide inundation hazard mapping. An initial DEM, a regolith depth map, and the location polygon of the landslide source area are the only inputs required to run MWR to model the entire runout process. Runout relies on the principle of mass conservation and a set of topographic rules and empirical formulas that govern erosion and deposition. For the purpose of facilitating rapid calibration to a site, MWR includes a calibration utility that uses a Markov Chain Monte Carlo algorithm to automatically calibrate the model to match observed runout extent, deposition and erosion. Additionally, the calibration utility produces empirical probability density functions of each calibration parameter that can be used to inform probabilistic implementation of MWR. Here we use a series of synthetic terrains to demonstrate basic model response to topographic convergence and slope, test calibrated model performance relative to several observed landslides, and briefly demonstrate how MWR can be used to develop a probabilistic runout hazard map. A calibrated runout model may allow for region-specific and more insightful predictions of landslide impact on landscape morphology and watershed-scale sediment dynamics, and should be further investigated in future modelling studies.

1. Introduction

Over geologic timescales, landslides and their runout shape the topographic expression of mountain ranges and channel networks (e.g., Campforts et al., 2022; Korup, 2006; Larsen and Montgomery, 2012; Montgomery and Dietrich, 1988). Over more pragmatic engineering and environmental risk management timescales, landslides and their runout can inundate and destroy infrastructure (e.g., Kean et al., 2019) but also support numerous ecosystem

35 benefits, including carbon and nutrient transport from hillslopes to channels and the creation of riparian habitat (Benda
36 et al., 2003; Bigelow et al., 2007; Goode et al., 2012). Therefore, explicit representation of landslide runout is a
37 necessary component of: (1) landslide inundation hazard assessments, with emphasis on inundation extent and flow
38 depth (e.g., Frank et al. 2015; Han et al., 2015); (2) watershed sediment yield models, with emphasis on the
39 mobilization, deposition and type of sediment carried by the landslide (e.g., Bathurst and Burton, 1998;
40 Istanbuluoglu, et al., 2005); and (3) landscape evolution models, with emphasis on topographic change prediction
41 (e.g., Tucker and Bras, 1998; Istanbuluoglu and Bras, 2005; Campforts et al., 2022);

42 Landslide runout processes can be generalized into three phases: initiation, erosion, and deposition. After a landslide
43 initiates, it may break apart and flow as a relatively dry debris slide, or it may mix with surface runoff to become a
44 debris flow. The mobility of the mass wasting material and resulting erosion/deposition pattern often varies as a
45 function of runout topography and initial relief and size of the landslide (Iverson, 1997). Mobility may also be
46 impacted by substrate liquefaction (Hungar and Evans, 2004) and landslide basal cataclasis (Shaller et al. 2020). As
47 the runout material moves downslope, flow depth varies as a function of channel width (Kean et al, 2019), which in
48 turn impacts erosion rates (Schürch et al. 2011). Theoretical, field and laboratory observations indicate that erosion
49 rates may also depend on the moisture content of the channel bed (Iverson, 2012; McCoy et al. 2012), flow grain size
50 (Egashira et al., 2001) and granular stress within the flow (Capart et al, 2015). The slope at which deposition begins
51 is controlled by the grain to water ratio and friction angle of the slide material (Takahashi, 2014; Major and Iverson,
52 1999; Zhou et al., 2019) but the friction angle of the material may vary as a function of the grains in the flow and
53 fluidization of the flow material (Hutter et al., 1996). Lateral levees often form along the edges of the flow (Major,
54 1997; Whipple and Dunne, 1992; Shaller et al., 2020) and deposition at the distal end of the flow may occur as layered
55 accretion (Major, 1997) or as the emplacement of a single, massive deposit (Shaller et al., 2020). If the water content
56 of the runout material is high enough, as the solid fraction of the distal end of the flow compresses, the water is
57 squeezed out and may continue as an immature debris flow (sensu Takahashi, 2014) or intense bedload (sensu Capart
58 & Fraccarolo, 2011), extending the runout distance (e.g., Shaller et al. 2020).

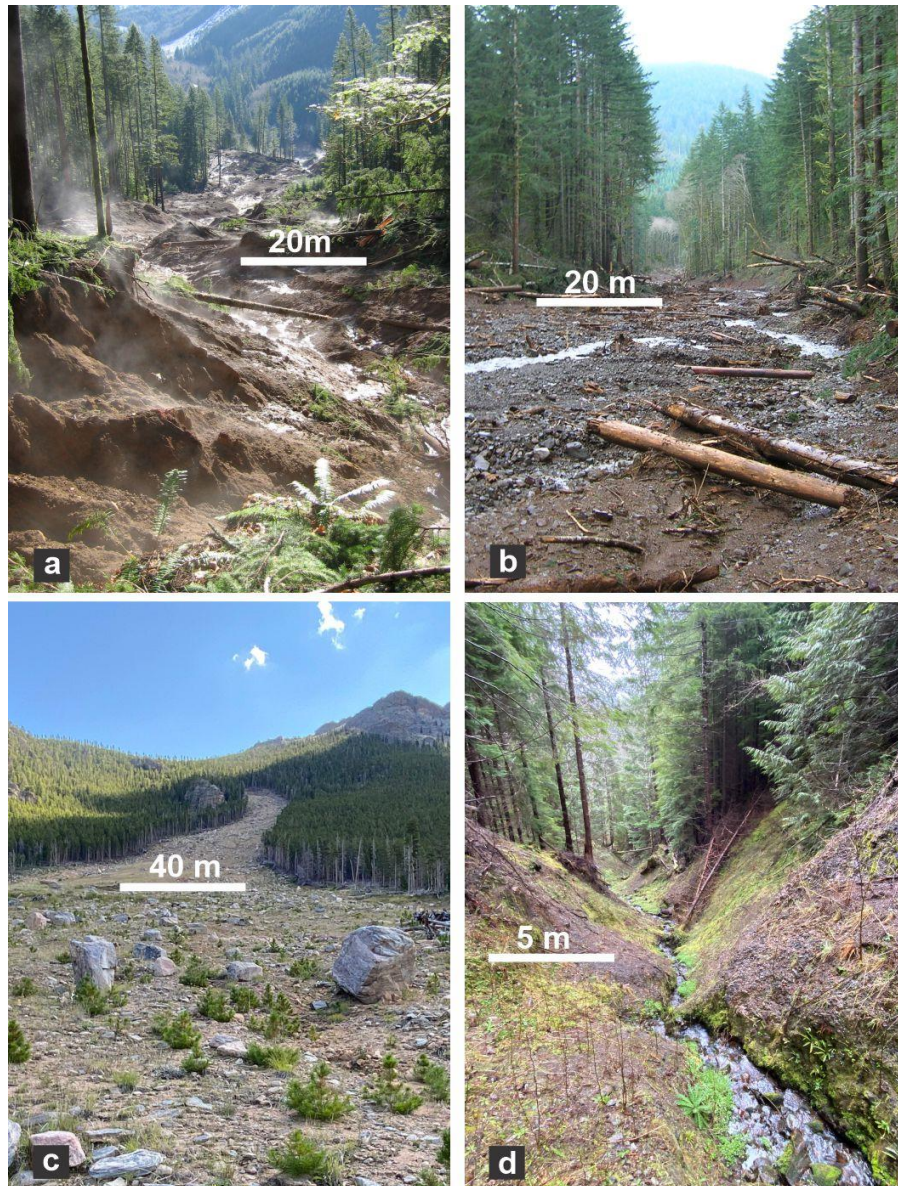
59 Landslide inundation hazard models aim to accurately predict the runout extent and/or flow depths of a runout event
60 and may include some or most of the above processes in the model. Example models include: (1) site-specific-
61 empirical/statistical models that use simple geometric rules and an estimate of the total mobilized volume (initial
62 landslide + eroded volume) or a growth factor (e.g., Reid et al. 2016); (2) detailed, continuum-based mechanistic
63 models, which conceptualize the runout process as a single-phase or multiphase flow using the depth-integrated
64 Navier-Stokes equations for an incompressible, free-surface flow (i.e., shallow water equations; Frank et al, 2015;
65 Han et al., 2015; Iverson and Denlinger, 2001; Medina et al., 2008) and often (though not always) require pre-
66 knowledge of the total mobilized volume (e.g., Barnhart et al., 2021; Han et al. 2015); (3) reduced complexity flow-
67 routing models that use rule-based abstractions of the key physical processes that control the flow (Clerici and Perego,
68 2000; Guthrie and Befus, 2021; Gorr et al., 2022; Han et al., 2017, 2021; Horton et al., 2013; Liu et al, 2022) and are
69 typically implemented using just the initial landslide location and volume but often rely on heavy, site specific
70 parameterization and; (4) hybrid modelling approaches that combine mechanistic models with empirical and reduced

71 complexity approaches (D'Ambrosio et al., 2003; Iovine et al., 2005; Lancaster et al., 2003; McDougall and Hungr
72 2004).

73 For landscape evolution and watershed sediment yield applications (herein referred to as watershed sediment models,
74 WSMs), the runout model must be scalable in both space and time, and capable of modelling the entire runout process
75 given an internally modelled initial landslide body (e.g. Tucker and Bras, 1998; Doten et al 2006; Campforts et al.
76 2022). As such, computationally efficient and parsimonious reduced complexity runout models that evolve the terrain
77 and transfer sediment are often preferred in WSMs, however with simplifications that can restrict model ability to
78 accurately replicate observed inundation extent or depositional patters. Such simplifications include omitting debris
79 flow erosion and bulking in runout channels, limiting flow to only a single cell in the steepest downstream direction,
80 and assuming debris flows only occupy the width of a single cell (e.g., Tucker and Bras, 1998; Istanbuluoglu and
81 Bras, 2005) or link of a channel network (Benda and Dunne, 1997).

82 To bridge the scalable functionality of WSMs with the predictive accuracy of landslide inundation hazard models,
83 without the computational overhead of a detailed mechanistic representation of the runout process, or difficult
84 parameterization typical of other models, we developed a new, reduced complexity landslide runout model, called
85 MassWastingRunout (MWR). MWR models landslide runout starting from the source area of the landslide, making it
86 easily compatible with WSMs that internally determine the initial landslide body size and location. MWR tracks
87 sediment transport and topographic change downstream, and evolves the attributes of the transport material. MWR
88 can be calibrated by adjusting just two parameters (S_c and q_c , described in Section 2) and is augmented with a Markov
89 Chain Monte Carlo (MCMC) calibration utility that automatically parameterizes model behavior to observed runout
90 characteristics (e.g., erosion, deposition, extent). MWR also includes a built-in utility called MWR Probability,
91 designed for running an ensemble of simulations to develop probabilistic landslide runout hazard maps.

92 In this paper, we present the conceptualization and numerical implementation of the MWR model (Section 2), describe
93 the calibration utility and its probabilistic implementation (Section 3) and demonstrate basic model response to
94 topographic convergence and slope on a series of synthetic terrains (Section 4). Event-scale applications to replicate
95 observed runout extent, sediment transport, and topographic change at four topographically and geologically unique
96 field sites (see Figure 1) are discussed (Section 5). We test MWR's predictive ability using the parameterization of
97 one site to predict runout hazard at a nearby site and show a brief example of Monte Carlo model runs to determine
98 runout probability from initial landslide source areas defined by an expert-determined potentially unstable slope or a
99 hydrologically-driven landslide hazard model (Section 6). We conclude with a short summary of MWR model
100 performance and discuss how a calibrated MWR can be incorporated into WSMs.



101

102 **Figure 1:** Example landslides used to evaluate calibrated MWR performance: (a) Cascade Mountains, WA: a large debris avalanche
 103 over steep, broadly convergent terrain (photo credit: Stephen Slaughter). (b) Black Hills, WA: large debris flows over a broadly
 104 convergent, gently sloped valley (photo credit: Stephen Slaughter). (c) Rocky Mountains, CO: a moderate sized debris avalanche
 105 over steep, unconfined to divergent hillslope. (d) Olympic Mountains, WA: small debris flows in steep, highly convergent channels.
 106 Image scale varies with depth, but approximate scale of the image is indicated at the location of the scale bar.

107 **2. Description of the MassWastingRunout model**

108 **2.1 Overview of the cellular-automaton modelling approach**

109 MWR is coded as a discrete cellular automaton (CA) model. CA models apply a set of equations or rules (deterministic
 110 or probabilistic) to individual cells of a grid to change the numerical or categorical value of a cell state (e.g., Codd,
 111 1968). In earth sciences, CA models are widely used to model everything from vegetation dynamics (e.g., Nudurupati
 112 et al., 2023) to lava flows (e.g., Barca et al., 1993) to geomorphic transport, in which gravitationally directed erosion

113 and depositional processes modify a digital elevation model (DEM) representation of a landscape (e.g., Chase, 1992;
114 Crave & Davy, 2001; Murray & Paola, 1994; Tucker et al., 2018). Existing CA-based landslide runout models include
115 models by Guthrie and Befus (2021), D’Ambrosio et al. (2003) and Han et al. (2021). In all of these models, runout
116 behavior is controlled by topographic slope and rules for erosion and deposition but conceptualization and
117 implementation differ.

118 In MWR, mass continuity is central to model conceptualization. Of the wide range of processes described in the
119 introduction that control observed runout, MWR explicitly represents erosion, deposition, and flow resistance due to
120 debris size and vegetation. Material exchange between the runout material and underlying terrain as well as flow
121 resistance determines runout extent and landscape evolution. Model rules are designed such that they can be
122 parameterized from field measurements. Finally, in MWR, most computations occur only at the location of moving
123 debris, in a manner analogous to the “mobile” cellular automaton implementation of Chase (1992).

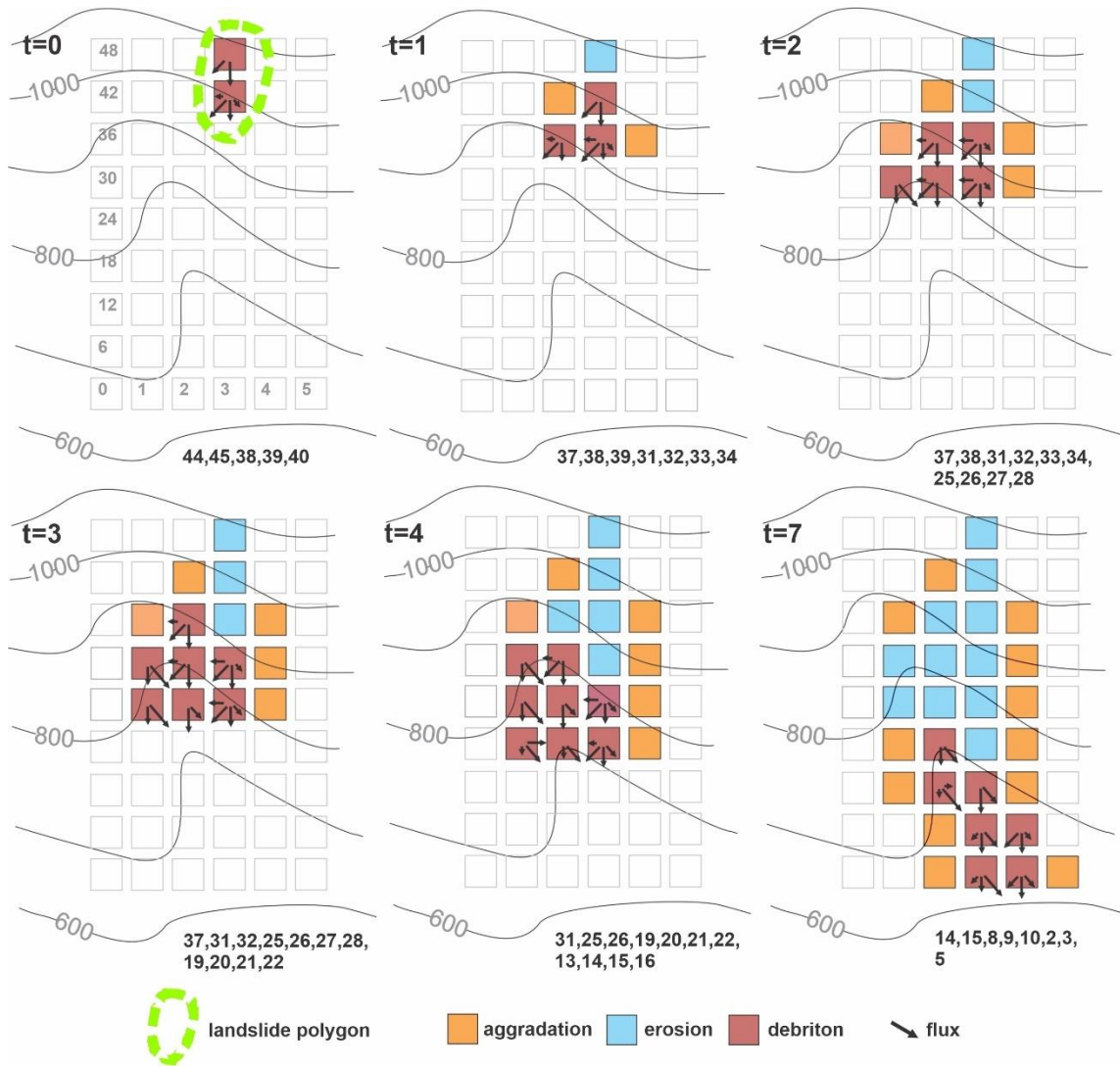
124 Chase (1992) modelled precipitation-driven surface erosion by randomly placing single packets of precipitation on a
125 DEM, which then moved from higher elevation to lower elevation grid cells, eroding and transporting sediment as a
126 function of the slope between the cells. The individual packets of precipitation were referred to as precipitons. In
127 MWR, since we route the downslope progression of debris from a specified mass wasting source area, we refer to
128 these packets of debris as “debritons”. The debritons represent debris flux, here defined as a volume of debris
129 transferred per model iteration per grid-cell area, [$\text{m}^3/\text{m}^2/\text{iteration}$] and are equivalent to the flow depth in the cell.

130 The present implementation of the MWR algorithm is coded in Python and developed as a component of the Landlab
131 earth surface modeling toolkit (Barnhart et al., 2020; Hobbey et al., 2017). MWR uses the Landlab raster model grid,
132 which consists of a lattice of equally sized, rectangular cells. Topographic elevation, derived topographic properties
133 like slope and curvature, and other spatially varying attributes such as regolith depth and grain size, are recorded at
134 nodes in the center of each cell (see Figure 5 of Hobbey et al., 2017). In the subsequent sections we describe the model
135 theory. All parameters and variables used in the theory are listed in the Notation section.

136 **2.2 Mobilization of the initial mass wasting source material (Algorithm 1):**

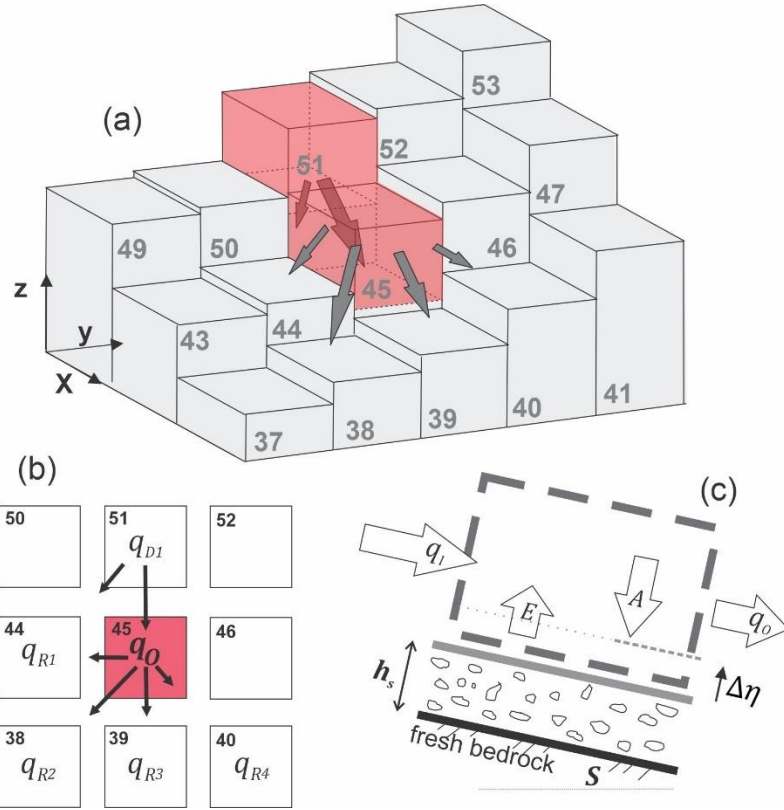
137 To initiate MWR, the user provides maps of initial topography, regolith depth, and the location and depth of the mass
138 wasting source material (e.g., the initial landslide body). Each raster model grid node in the mass wasting source
139 material is designated as a debriton (Figure 2, iteration $t = 0$) with a magnitude equal to the mass wasting source
140 material depth and basal elevation equal to the initial topography minus the mass wasting source material depth. The
141 basal elevation can be thought to represent the rupture or slip surface of the source material and the redistribution
142 (flux) of each debriton to its downslope nodes (receiver nodes) is determined as a function of the slope of the slip
143 surface. At the lowest-elevation debriton of the source material, flux to its downslope nodes is determined using the
144 surface slope of the initial DEM (see flow direction of lowest node in Figure 3a). This implementation helps to ensure
145 that the lowest-elevation debriton in the mass wasting source material moves downslope and movement of upslope
146 debritons are impacted by the geometry of the mass wasting source material. For example, the receiver nodes of the
147 lowest-elevation debriton in the landslide illustrated in Figure 2 (iteration $t = 0$, detailed in Figure 3a) would be
148 identified as those among the eight neighboring nodes whose initial topographic elevation was less than the initial

149 topographic elevation of the node while for the debriton at node 51, the receiver nodes would be identified as those
 150 among the eight neighboring nodes whose topographic elevation is less than the topographic elevation of the terrain
 151 underlying the debriton (the slip surface).



152

153 **Figure 2.** Illustration of initial mass wasting release and runoff down a steep, convergent slope. Variable t indicates model iteration
 154 (not time). Notice how the flow elongates and widens as the model progresses and the number of receiver nodes (numbers listed at
 155 bottom of each panel) and quantity of mobilized material increase. -



156

157 **Figure 3.** (a) Three-dimensional illustration of iteration $t = 0$ in Figure 2, showing initial source material nodes (represented by red
 158 cells) and flux towards downslope nodes. (b) Distribution of q_0 to downslope nodes 38, 39, 40 and 44; (c) illustration of mass
 159 continuity applied to any node that receives a debriton.

160

161 2.3 Flow routing and rules for erosion, deposition and resistance (Algorithm 2)

162 Algorithm 2 is essentially the runout model. It determines how each debriton traverses and modifies the landscape.
 163 After receiver nodes from the first model iteration are determined in Algorithm 1 (iteration $t=0$), Algorithm 2 is
 164 repeatedly implemented until all material has deposited (i.e., there are no debritons). Each debriton moves one grid
 165 cell per model iteration, the larger the landslide size, the more iterations necessary to evacuate the landslide. As each
 166 debriton moves, it may erode or aggrade the landscape, impacting the movement of any upslope debritons. As is
 167 common with other reduced complexity models, we assume that inertial effects have negligible impact on flow
 168 behavior (i.e., the kinematic flow approximation). The downslope redistribution of a debriton or flux to each of a
 169 node's i -th receiver nodes (q_{R_i}) is determined as a function of topographic slope (slope of terrain under the debriton)
 170 using the Freeman (1991) multiple flow direction algorithm:

$$171 \quad q_{R_i} = q_0 \frac{S_i^a}{\sum_{i=1}^{Nr} S_i^a} \quad (1)$$

172 where q_0 is the total out-going flux from the node and has units of depth [m] per model iteration, Nr is the number
 173 of receiving nodes, i is the index for each receiver node (e.g., $i = 1, 2 \dots Nr$) and S_i is the underlying topographic

174 slope to the i -th receiver node (Figure 3b). The Freeman (1991) multiple flow direction algorithm is a commonly used
 175 approximation for two-dimensional flow, and in this implementation it is handled by a pre-existing Landlab flow-
 176 routing component. The exponent a controls how material is distributed to downslope nodes, with higher values
 177 causing narrower flow (Holmgren 1994). In a braided river cellular-automaton model, Murray and Paola (1997) used
 178 an approximation for turbulent shallow water flow to justify $a = 0.5$ (which is the exponent on the slope factor in
 179 channel friction laws). For our application, we found MWR provided a closer fit to observed mass wasting runout if
 180 $a = 1$, suggesting that the material behavior is more similar to linear-viscous shear flow than to wall-bounded turbulent
 181 shear flow (e.g., as the runout debris flows downslope, it tends to spread less than shallow turbulent water). The total
 182 incoming flux (again, in units [m] per model iteration) towards a given node (q_I), is determined by summing the flux
 183 from each of the node's donor nodes:

$$184 \quad q_I = \sum_{j=1}^{Nd} q_{D_j} \quad (2)$$

185 Where Nd is the number of donor nodes, and q_{D_j} is the flux from node D_j (the j -th donor node, $j = 1, 2, \dots, Nd$; Figure
 186 3b).

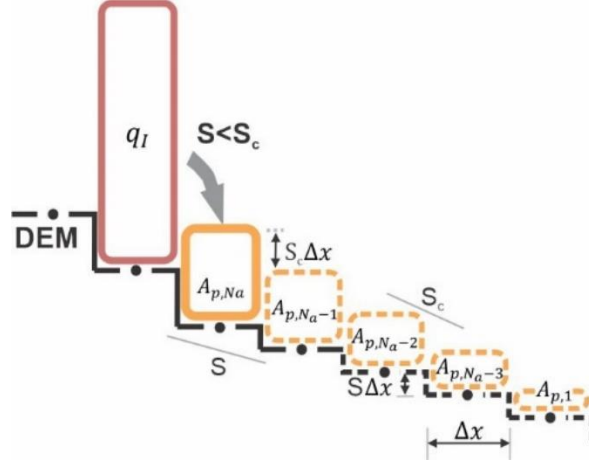
187 As noted by Tucker and Hancock (2010), the flow depths calculated from two-dimensional flow approximations like
 188 (1) can be influenced by the grid-size used to represent the terrain and depending on terrain slope and convergence,
 189 neglect of pressure and momentum forces may lead the model to underestimate or overestimate flow width in some
 190 circumstances. Rengers et al. (2016) noted that this same issue occurs when using a kinematic wave approximation of
 191 the shallow water equations because the kinematic wave approximation lacks a pressure term that would normally
 192 allow the modelled water surface to spread out. We consider flow depths determined from (2) as meaningful in the
 193 sense that they vary as a function of flux but less meaningful in the sense that they are affected by the limitations noted
 194 above. Furthermore, for the purpose of determining flow-depth-dependent erosion rates described later in this paper,
 195 and to provide a simplified representation of the effect of pressure forces, we constrain flow depths to no more than a
 196 maximum flow as:

$$197 \quad h = \min(h_{max}, q_I) \quad (3)$$

198 Where h_{max} is an effective upper limit to flow depth, that in practice can be approximated as the maximum observed
 199 flow depth, as inferred from field indicators or assigned based on expert judgement (See Section 5) and h is the
 200 corrected flow depth used to calculate flow shear stress. This correction allows erosion rates to vary with flux but
 201 prevents unreasonably large values. This flow depth correction does not violate the conservation of mass and runout
 202 mass balance, as h is only used to calculate flow shear stress.

203 To determine aggradation (A) at a node, we use a critical slope (S_c) constraint that permits computationally-rapid
 204 distribution of q_I over multiple nodes. Critical slope constraints or rules are common to many reduced complexity and
 205 landscape evolution models. Chen et al. (2023) showed that when flow inertia can be ignored, S_c can be approximated
 206 from the surface slope of observed deposits. Several landscape evolution models use a S_c -based nonlinear, nonlocal
 207 aggradation scheme (e.g., Campforts et al., 2020; Carretier et al., 2016) but when this rule is implemented with the
 208 debriton framework described above, unreasonably tall deposits result when q_I is large and slope at the node (S) \ll

209 S_c . To resolve this problem, aggradation depth can be limited to $A \leq S_c \Delta x$, (where Δx grid cell length), but we found
 210 that this constraint results in long deposits that parallel the underlying slope when q_I is large. Instead, MWR computes
 211 the aggradation depth at a node assuming that the aggradation will spread over N_a nodes until all of q_I is deposited
 212 and that the surface slope of the overall deposit will be equal to S_c , as shown in Figure 4 and described as follows.



213
 214 **Figure 4.** Illustration of aggradation rule used in MWR when q_I is assumed to spread over 5 nodes ($N_a = 5$). Solid
 215 yellow box indicates aggradation amount at a given node. Dashed yellow boxes and lines indicate the geometry of
 216 assumed the aggradation beyond the node. Dots along DEM surface are nodes.

217 Aggradation at a node is determined as:

$$218 \quad A = \begin{cases} 0, & S \geq S_c \\ \min(A_{p,N_a}, q_I), & S < S_c \end{cases} \quad (4)$$

219 Where S is the steepest slope to the node's eight neighbouring nodes, A_{p,N_a} is a potential aggradation depth necessary
 220 to form a deposit that: (1) begins at the node and spreads over N_a consecutive nodes; (2) has a total volume equal to
 221 $q_I \Delta x^2$; (3) a surface slope equal the critical slope S_c and; (4) an underlying topographic slope equal to the steepest
 222 slope at the node and assumed constant over the N_a consecutive nodes of deposition. From this assumed deposit, we
 223 can analytically define A_{p,N_a} and N_a as a function of q_I , S_c and S as follows:

224 First, q_I , calculated from (2), can be used to calculate $A_{p,i}$ by expressing q_I as the sum of the N_a deposits that make
 225 up the overall deposit as:

$$226 \quad q_I = \sum_{i=1}^{N_a} A_{p,i} \quad (5)$$

227 where $A_{p,i}$ is the i -th deposition amount in the deposit and $i = 1$ is the last node of deposition ($A_{p,1}$; see Figure 4).
 228 Since we assume the deposit slope and underlying topographic slope are uniform, the deposition amount at any of the
 229 N_a nodes can be determined from $A_{p,1}$ as:

$$230 \quad A_{p,i} = A_{p,1} + (i - 1)\Delta x(S_c - S) \quad (6)$$

231 From (6) we can re-write (5) as a function of $A_{p,1}$ and rearrange to define $A_{p,1}$ as a function of q_I :

232
$$A_{p,1} = \frac{1}{N_a} q_I - \frac{N_a - 1}{2} \Delta x (S_c - S) \quad (7)$$

233 Substituting (7) into (6) and solving for $i = N_a$, we get an expression for A_{p,N_a} :

234
$$A_{p,N_a} = \frac{1}{N_a} q_I + \frac{N_a - 1}{2} \Delta x (S_c - S) \quad (8)$$

235 Equation (8) can be rearranged into a quadratic equation and solved for N_a as:

236
$$N_a = \frac{-A_{p,1} + \frac{1}{2} \Delta x (S_c - S) \pm \sqrt{\left(A_{p,1} - \frac{1}{2} \Delta x (S_c - S) \right)^2 + 2 \Delta x (S_c - S) q_I}}{\Delta x (S_c - S)} \quad (9)$$

237 We use (8) to solve for A_{p,N_a} and (9) to solve for N_a assuming $A_{p,1} = 1/2 \Delta x S_c$ and rounding the positive solution to
 238 the nearest integer. When implemented using a single debriton, released on a two-dimensional hillslope as illustrated
 239 in Figure 4, the debriton deposits over N_a nodes at a uniform slope equal to S_c . When implemented on an actual three-
 240 dimensional terrain, the interaction between multiple debritions in multiple directions creates a complex deposit whose
 241 slope changes with S_c .

242 To determine erosion depth (E) [m/iteration], we constrain E to the lesser of a potential erosion depth, h_e , and local
 243 regolith depth, h_r :

244
$$E = \min (h_r, h_e) \quad (10)$$

245 where h_e is computed as a function of the basal shear stress of the flow, τ [Pa], (Equations 12 and 13) and the critical
 246 shear stress (τ_c) of the regolith at the node [Pa]:

247
$$h_e = k(\tau - \tau_c)^f \quad (11)$$

248 The coefficient k is an erodibility parameter [m/Pa^f]. Stock and Dietrich (2006) showed that k encapsulates substrate
 249 properties. If h_e is used to represent erosion over geomorphic time scales, with repeated debris flow occurrences in a
 250 single model iteration, k becomes associated with debris flow length and frequency (Perron, 2017). In our application
 251 since we are modelling the erosion associated with a single runout event, as represented by the downslope movement
 252 of the debritions, the coefficient k therefore needs to scale h_e on the order of the average erosion depth caused by a
 253 single debriton. Using this logic, k can be computed using the observed average erosion depth and an estimated length
 254 of the runout material that caused the erosion. Further details on how we determine k from observed runout are
 255 included in the Appendix. The exponent f controls the non-linearity of h_e with shear stress. Many authors (Chen &
 256 Zhang, 2015; Frank et al., 2015; Shen et al., 2020) use a value of 1 for f but field measurements by Schürch et al.
 257 (2011) (see their Figure 3) suggest that f may be less than 1 if τ is assumed to vary linearly with flow depth,
 258 particularly at flow depths greater than 3 meters.

259 MWR includes two options for defining τ : (1) a quasi-static basal shear stress approximation or (2) a grain-size-based
 260 shear stress approximation. The quasi-static basal shear stress approximation (e.g., Takahashi, 2014) is defined as:

261
$$\tau = \rho g h \sin \theta \quad (12)$$

262 where ρ is the density of mass wasting material (grain and water mixture) [kg/m^3], g is gravity [m/s^2], h is the adjusted
 263 flow depth described in (3) and θ is the topographic slope ($\tan^{-1}(S)$) measured in degrees.

264 The grain-size-based shear stress approximation is defined using an empirical formula by Bagnold (1954):

$$265 \quad \tau = \sigma \tan \varphi \quad (13)$$

266 Where σ is normal stress [Pa], φ is the collision angle between grains, measured from the vertical axis (See Bagnold,
 267 1954), with a value of $\tan \varphi$ typically equal to 0.32. Stock and Dietrich (2006) defined σ as:

$$268 \quad \sigma = \cos \theta v_s \rho_s D_s^2 \left(\frac{du}{dz} \right)^2 \quad (14)$$

269 Where v_s is the volumetric solids concentration, ρ_s is density of the solids [kg/m^3], u is flow velocity [m/s], z is depth
 270 below the flow surface [m], du/dz is the shear strain rate [1/s] and D_s is the representative grain size [m]. Stock and
 271 Dietrich (2006) suggested that D_s corresponds to a small percentile of the coarsest fraction of the runout material (D_{88}
 272 to D_{96}) and they approximated du/dz as:

$$273 \quad \frac{du}{dz} = \frac{u}{h} \quad (15)$$

274 Solely for the purpose of computing du/dz , we approximate velocity at a node using a grain-size dependent empirical
 275 formula for debris flow velocity by Julien and Paris (2010) as:

$$276 \quad u = 5.75 u^* \log \left(\frac{h}{D_s} \right) \quad (16)$$

277 Where u^* is shear velocity ($\sqrt{gh \tan \theta}$). Substituting (16), (15), (14) and (13) into (11) yields a grain-size dependent
 278 approximation for h_e that mimics the non-linear erosion response to flow depth in Schürch et al. (2011). Additionally,
 279 this form of τ is advantageous because it permits landslide-driven erosion rates to scale with landslide grain size,
 280 which can vary by lithologic region (e.g., Roda-Boluda et al. 2018). As will be shown in Section 5, we obtained
 281 reasonable model calibration at multiple sites by defining D_s from the coarser grain sizes observed in the field at
 282 existing runout-deposits, road-cuts and tree-throw pits.

283 Once A [m] and E [m] have been determined, total out-going flux per iteration, q_o [m] is determined as (see Figure
 284 3c):

$$285 \quad q_o = \begin{cases} q_I - A + E, & q_I \geq q_c \\ 0, & q_I < q_c \end{cases} \quad (17)$$

286 Where q_c is a threshold flux for deposition. When $q_I < q_c$, q_I deposits and q_o becomes zero. The threshold flux q_c
 287 conceptually represents the flow depth below which flow resistance is large enough to cease the forward momentum
 288 of the flow, whether in the form of internal friction or friction due to vegetation and obstructions (e.g., large clasts or
 289 logs). The density and water content of q_I , A , and E are treated as uniform and surface runoff, such as channelized
 290 stream flow or hillslope-infiltration-excess runoff, that might mix with q_I . A , or E is ignored. Once q_I , A , q_o and E
 291 have been determined, change in elevation at a node ($\Delta\eta$) is calculated as:

$$292 \quad \Delta\eta = A - E \quad (18)$$

293 Attributes (e.g., grain size, organic content or any other attribute that is transferred in the flow) of the debriton and
 294 regolith are updated using a volumetric-weighted average approach. First, for each regolith attribute being tracked by
 295 the model, the attribute value delivered to a node from its donor nodes (ξ_D) is determined as:

$$296 \quad \xi_D = \frac{\xi_D \cdot \mathbf{q}_D}{q_I} \quad (19)$$

297 where \mathbf{q}_D is a vector containing all q_{D_j} sent to the node, ξ_D is a vector containing the incoming attribute values for
 298 each q_{D_j} , and q_I is the sum of incoming flux from donor nodes defined by (2).

299 Second, the attribute value sent from a node to its receiver nodes (ξ_R) is determined as:

$$300 \quad \xi_R = \frac{\xi_{t-1}E + \xi_D(q_I - A)}{q_O} \quad (20)$$

301 where ξ_{t-1} is the attribute value at the node before any aggradation (i.e., the previous iteration attribute value). Finally,
 302 the attribute value at the node, updated to account for erosion and aggradation (ξ) is:

$$303 \quad \xi = \frac{\xi_{t-1}(h_r - E) + \xi_D A}{A + h_r - E} \quad (21)$$

304 Regolith thickness (h_r) and topographic elevation (η) are updated at a node as:

$$305 \quad \eta = \eta_{t-1} + \Delta\eta \quad (22)$$

$$306 \quad h_r = h_{r,t-1} + \Delta\eta \quad (23)$$

307 Where η_{t-1} and $h_{r,t-1}$ are the topographic surface elevation and regolith thickness at the node from the previous
 308 model iteration. After regolith thickness and topographic elevation have been updated for each debriton, the multi-
 309 direction slope of the DEM, which is used for routing the debritons in the next model iteration, is recomputed from
 310 the topographic surface.

311 Using the above approach, debritons may become obstructed if they encounter a topographic pit or flat topography in
 312 the DEM. To allow a debriton to pass an obstruction, we rely on a simple work-around: upon encountering the
 313 obstruction, the debriton is directed to itself and some portion of the debris is deposited based on (4). At the end of
 314 the model iteration, the node elevation and slope are updated. During the next iteration, if the remaining mobile debris
 315 is no longer obstructed, it moves to its downslope node(s). If the node is still obstructed, it is again sent to itself until
 316 either all material has deposited or the elevation of the node exceeds that of its neighbour nodes, allowing the debriton
 317 to move downslope.

318 **3. Calibration and MWR probability**

319 **3.1 Calibration utility**

320 MWR includes an adaptive Markov Chain Monte Carlo (MCMC) calibration algorithm described by Coz et al. (2014)
 321 and Renard et al. (2006). The MCMC algorithm is implemented as a utility for MWR and identifies a single set of
 322 parameters that best match MWR output to an observed landslide runout dataset. The observed runout dataset can
 323 consist of a single or multiple landslides. Depending on user input, MWR simultaneously or sequentially models

324 runout from each landslide source area in one model run. To use the calibration utility, the user provides an initial
 325 (prior) guess of the parameter values and their respective probability distribution functions (PDF) that calibrate the
 326 MWR to a specific site. Then, the calibration utility randomly selects a set of trial parameter values (Λ) from the prior
 327 PDFs and runs MWR using Λ . Once the model has completed the run, the algorithm evaluates the posterior likelihood
 328 of the parameter set ($L(\Lambda)$) as a lumped index of model ability to replicate observed runout (described below) and the
 329 prior likelihood of the parameter set. After the first $L(\Lambda)$ has been determined, the utility selects a new set of
 330 parameters (Λ_{t+1}) by jumping some distance (described below) from each parameter in Λ space. Depending on the
 331 value of $L(\Lambda_{t+1})$, the algorithm either stays at Λ or moves to Λ_{t+1} . This Markov process is repeated a user-specified
 332 number of times. Jump direction is random, but the algorithm is adaptive because the jump distance changes depending
 333 on if $L(\Lambda_{t+1}) > L(\Lambda)$ occurs more than a user specified threshold value. For a detailed description of the algorithm
 334 see Coz et al. (2014).

335 The $L(\Lambda)$ index is estimated as the product of the prior probability of the selected parameter values, $p(\Lambda)$, and three
 336 other performance metrics as:

$$337 \quad L(\Lambda) = p(\Lambda) * \Omega_T * \frac{1}{\Delta\eta_E^2} * \frac{1}{Q_{sE}^2} \quad (24)$$

338 where Ω_T is the Lee-Salle index (Heiser et al., 2017) for evaluating model planimetric fit and $\Delta\eta_E$ and Q_{sE} are new
 339 dimensionless indices, proposed for this study (described below). The indice $\Delta\eta_E$ is the volumetric error of the
 340 modelled topographic change over the entire model domain normalized by the observed total mobilized volume (initial
 341 landslide body + erosion volume). The indice Q_{sE} is the mean-cumulative sediment export error along the modelled
 342 runout path normalized by the observed mean cumulative flow. Larger values of Ω_T and smaller values of $\Delta\eta_E$ and
 343 Q_{sE} indicate modelled runout more closely fits observed. Note that we add a value of 1 to Ω_T and use the squared-
 344 reciprocal values of $\Delta\eta_E$ and Q_{sE} in (24) so that the magnitude of $L(\Lambda)$ is always equal to or greater than zero and
 345 increases with improved fit. The metric Ω_T is written as:

$$346 \quad \Omega_T = \frac{\alpha - \beta - \gamma}{\alpha + \beta + \gamma} + 1 \quad (25)$$

347 where α, β and γ are the areas of matching, overestimated and underestimated runout extent, respectively.

348 The spatial index for volumetric error, $\Delta\eta_E$, is determined as:

$$349 \quad \Delta\eta_E = \sqrt{\frac{\sum_{i=0}^p [(\Delta\eta_{Oi} - \Delta\eta_{Mi})\Delta x^2]^2}{V^2}}. \quad (26)$$

350 Where V is observed total mobilized volume and p is the number of nodes in the area made up of the matching,
 351 overestimated and underestimated areas of runout extent and $\Delta\eta_{Mi}$ and $\Delta\eta_{Oi}$ are the modelled and observed
 352 topographic change [m] at the i -th node within that extent.

353 To calculate Q_{sE} , we first determine the cumulative export (flow) volume (Q_s) at each node, j along the runout profile,
 354 in a manner similar to the flow volume/mass balance curves in Fannin and Wise (2001) and Hungr and Evans (2004):

$$355 \quad Q_s = -\Delta x^2 \sum_{i=1}^{u_j} \Delta\eta_{i,j} \quad (28)$$

356 where $\Delta\eta_{ij}$ is the topographic change [m] at the i -th node located upstream of node j , and u_j is the total number of all
 357 nodes located upstream of j . Q_s is computed for both the observed and modelled runout path (Q_{sO} and Q_{sM}
 358 respectively) and Q_{sE} of a runout is determined as:

$$359 \quad Q_{sE} = \sqrt{\frac{\frac{1}{r} \sum_{j=1}^r (Q_{sO} - Q_{sM})^2}{\overline{Q_{sO}}^2}} \quad (29)$$

360 Where r is the number of nodes along the center line of the runout path, and $\overline{Q_{sO}}$ is the observed mean cumulative
 361 flow.

362 As will be detailed in Section 5, field estimates for S_c and q_c , vary over the length of the runout path. To account for
 363 the heterogeneity of S_c and q_c , we estimate prior distributions of potential S_c and q_c values from field/remote sensing
 364 measurements. Then, from model calibration to a DEM-of-Difference (pre-runout DEM subtracted from the post-
 365 runout DEM; DoD) using the calibration utility, we find single values of S_c and q_c that allow the modelled DoD to
 366 replicate the observed DoD .

367 We run the calibration utility using a single Markov chain of 2000 repetitions. At most sites, the model converged
 368 relatively quickly on a solution and we therefore didn't consider burn-in or evaluate convergence (e.g., Gelman et al.
 369 2021) and considered 2000 repetitions adequate. Future implementations of the calibration utility may include multiple
 370 chains, burn-in and a check for convergence. As a final note, many debris flow runout models are evaluated using Ω_T
 371 or variations of Ω_T alone (e.g, Gorr et al., 2022; Han et al., 2017) and the MWR calibration utility can also be run
 372 solely as a function of Ω_T . However, we found that calibration based on Ω_T (i.e., runout extent) alone results in high
 373 parameter equifinality (e.g., Beven 2006); multiple parameter sets result in an equally calibrated model as evaluated
 374 by Ω_T . As such, we recommend calibrating debris flow/ landslide runout models to an observed DoD. If repeated lidar
 375 is available, a DoD can be obtained from before and after scans of the observed runout event. Alternatively, a DoD
 376 can be created by hiking the observed runout event and mapping field-interpreted erosion and deposition depths.
 377 Additional details on how we prepared DoDs for multiple sites are included in the Supplementary Material.

378

379 **3.2 Mapping landslide runout hazard**

380 MWR includes an additional utility called MWR Probability that produces landslide runout probability maps. MWR
 381 Probability repeatedly runs MWR a user specified Np times, each repetition with a different, randomly sampled
 382 parameter set from the posterior parameter PDFs produced by the calibration utility. MWR Probability includes three
 383 options for specifying the initial mass wasting source material: (1) a user-provided landslide source area polygon(s)
 384 based on field and/or remote sensing observations; (2) a user-defined hillslope susceptible to landslides (e.g.,
 385 potentially unstable slope), where landslide area and location are randomly selected within, but no larger than the
 386 hillslope; this option is useful when the extent of a potential landslide is unknown; and (3) a series of mapped landslide
 387 source areas within a watershed, as determined by an externally run Monte Carlo landslide initiation model (e.g.,
 388 Hammond et al. 1992; Strauch et al., 2018) ; this option is useful for regional runout hazard applications. If using

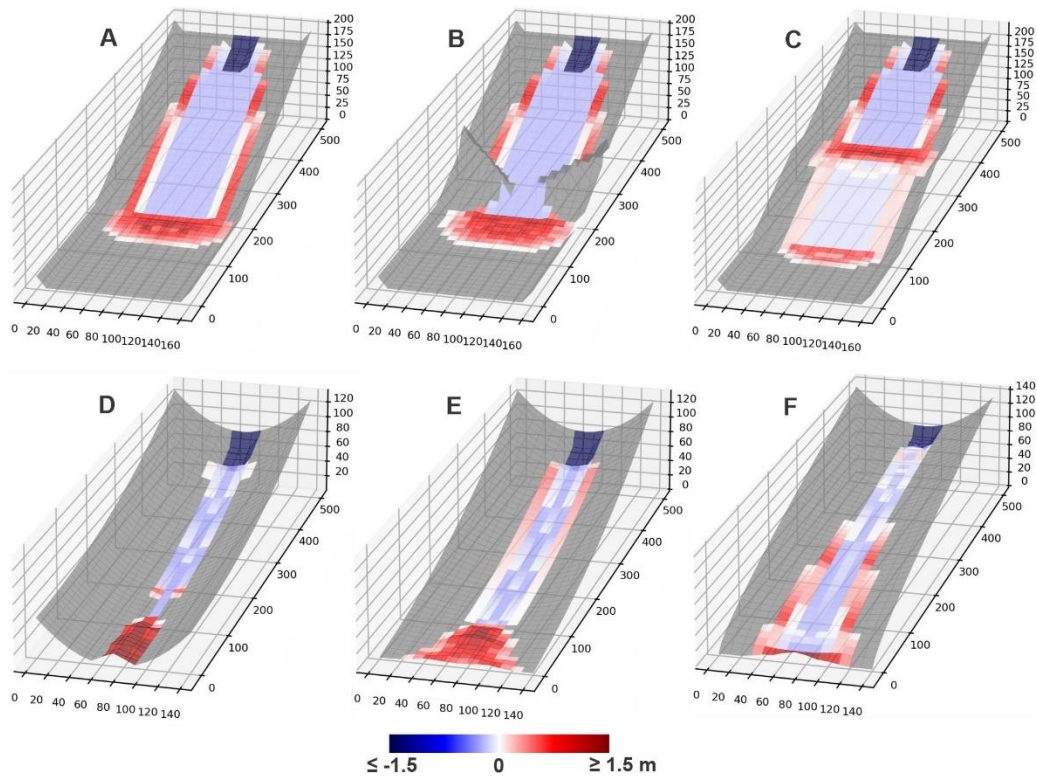
389 Option 1, modelled runout probability represents uncertainty in MWR parameterization. If using Option 2 or 3,
390 modelled runout probability reflects uncertainty in both MWR parameterization and landslide location and size.
391 For all three run options, each model iteration begins with the same initial topography. After Np model simulations,
392 Np different versions of the post-runout landscape are created and, probability of runout at each node is determined
393 as:

$$394 \quad P(\Delta\eta) = \frac{\#(|\Delta\eta| > 0)}{Np} \quad (30)$$

395 where $\#(|\Delta\eta| > 0)$ is the number of times topographic elevation at a node changes as a result of erosion or deposition
396 from the Np model runs. Probability of erosion or aggradation can be determined by replacing the numerator in (30)
397 with $\#(\Delta\eta < 0)$ or $\#(\Delta\eta > 0)$ respectively.

398 **4. Basic model behavior**

399 We evaluate basic model behavior using a series of virtual experiments. The virtual experiments consist of six
400 synthetic terrains including: (A) a planar slope that intersects a gently sloped plane ($S = 0.001$), (B) a planer slope
401 with a constriction, that intersects a gently-sloped plane, (C) a planar slope that has a bench mid-slope and then
402 intersects a gently-sloped plane; (D) a concave up, uniform-convergence slope; (E) a concave up, variable-
403 convergence slope that widens (convergence decreases) in the downslope direction; (F) a convex up, variable-
404 convergence slope that widens (convergence decreases) in the downslope direction. On each terrain, a 30-meter wide,
405 50-meter long and 3-meter deep landslide is released from the top of the terrain. All six terrains are covered by a 1-
406 meter thick regolith and use the same parameter values ($S_c = 0.03$, $q_c = 0.2$ m, $k = 0.01$, $D_s = 0.2$ m). Each terrain is
407 represented using a 10-m grid. Experiment results are shown in Figure 5.



408

409 **Figure 5.** Shaded, 3-D visualizations of model response to six different synthetic terrains, colored according to the
 410 DoD of the final runout surface. Shading is to scale. Red indicates a positive change in the elevation of the terrain
 411 (aggradation) and blue indicates a negative change (erosion). The 3-D visualization of the DoD is exaggerated by a
 412 factor of 5 to make visible in figure. Grid size is 10 meters.

413 On Terrain A, the landslide spread as it moved downslope and formed levees along the edge of the runout path. The
 414 width of the spread was a function of the multiple flow direction algorithm and resistance along lateral margins of the
 415 runout as represented by q_c . At the slope break at the base of the slope, the material deposited at an angle controlled
 416 by S_c . On Terrain B, the flow initially eroded and deposited identical to the first but near the slope break, the
 417 topographic constriction forced flow depth to increase and exceed q_c , minimizing the formation of levees (because
 418 $q_0 > q_c$) and resulted in a slightly larger deposit at the base of the slope. On Terrain C, landslide runout was again
 419 initially identical to the runout on Terrain A; however, upon intersecting the mid-slope bench, most of the runout
 420 material deposited. A small, thinner portion did continue past the bench but eroded at a lower rate than the initial slide
 421 upslope of the bench. Upon intersecting the flat surface at the base of the hillslope, the runout material deposited.

422 On Terrain D, the landslide and its runout were confined to the center of convergent terrain and only deposited once
 423 the slope was less than S_c . The slide never widened because the uniformly convergent channel shape prevented
 424 spreading and the narrower flow width maintained a higher flow depth, which prevented the formation of levees. On
 425 Terrain E, the landslide again deposited once slope was less than S_c but because topographic convergence of Terrain
 426 E decreases in the downslope direction, as the runout material moved downslope, the deposit spread more than on
 427 Terrain D, which caused thinner flow and deposition along margins of the runout path. On the final terrain, Terrain F,

428 slope is always greater than S_c so deposition was limited to levees along the edge of the flow that formed as the runout
429 spread in response to decreasing convergence.

430 MWR model behavior can be summarized as follows. The displacement and deposition of landslide material predicted
431 by MWR responds to topography in a reasonable manner: Flow width increases as convergence decreases (e.g, Terrain
432 F), which in turn reduces flow depth. Lower flow depths cause lower erosion rates and reduce aggradation extent.
433 Conversely, modelled flow depth increases when convergence increases (e.g., Terrain B). Where the flow encounters
434 broadly convergent or planer slopes, lateral levee deposits form, a common feature of landslides reported in the
435 literature and at sites reported here (see Section 5) that detailed mechanistic models can struggle to reproduce (e.g.,
436 Barnhart et al, 2021).

437 We did not attempt to compare MWR modelled flow with the output of shallow-water-equation based models or
438 observed granular flows (e.g., Medina et al, 2008; McDougall and Hungr, 2004; Iverson and Denlinger, 2001; Han
439 et al., 2015). The cellular automaton representation in MWR does not model the time-dependent evolution of debris
440 flow velocity and depth, and conceptually moves debris instantaneously at each iteration, as driven by changes in the
441 evolving topographic elevation field. Because of that, only the final outcome (modelled runout extent, sediment
442 transport and topographic change) of MWR can be compared with other models or observed runout, which we do in
443 the next section. Also, as described in Section 2.3, behaviour of the multiple flow direction algorithm does vary with
444 grid size. Using a coarser or finer grid, without adjusting model parametrization, could potentially change how wide
445 the landslide spreads.

446 **5. Model Validation:**

447 **5.1 Overview**

448 In this section, we demonstrate the ability of a calibrated MWR to replicate observed runout extent, sediment transport
449 and topographic change at field sites located in the western USA and summarize model calibration results with an
450 evaluation of MWR calibration relative to terrain attributes of the observed runout paths. Note that simply calibrating
451 a model to match field data does not constitute a satisfactory test of model predictive ability (Iverson, 2003). Strategic
452 testing, which involves calibrating the model to one site or period of time and then running the calibrated model at a
453 separate site or period of time (Murray, 2013), is a better indicator. Two of our validation sites, the Cascade Mountain
454 and Olympic Mountain sites, include two separate landslides and subsequent runout and we test model predictive
455 ability at these sites in Section 6.

456 Calibrated model performance is demonstrated at the following field sites (see Figure 6a for locations and observed
457 runout extent): (1) two runout events over the same hillslope in the Cascade Mountains (Washington state [WA],
458 USA): a large debris avalanche in 2009 (Cascade Mountains, 2009) and a moderately-sized debris flow in 2022
459 (Cascade Mountains, 2022) that inundated and flowed within a first-to-second order channel until perpendicularly
460 intersecting a narrow river valley several hundred meters below the landslide (Figure 1a); (2) debris flows in the Black
461 Hills (WA) sourced from a small failure along the toe of a deep-seated landslide (Black Hills, South) and a moderately-
462 sized debris avalanche from a large road fill (Black Hills, North) that flowed several kilometers along a relatively

463 wide, broadly convergent channel before stopping (Figure 1b); (3) a single, moderately-sized debris avalanche in the
 464 Rocky Mountains (Rocky Mountains), the majority of which flowed several hundred meters over a broadly convergent
 465 to divergent hillslope in Colorado (Figure 1c); and (4) a 30-year chronology of small landslides and subsequent debris
 466 flows in the Olympic Mountains (WA) in steep, highly convergent channels that flowed well over a kilometer and
 467 coalesced into a single runout deposit in a dendritic, channelized watershed (Olympic Mountains; Figure 1d). All
 468 landslides initiated during heavy rainfall or rain-plus-snowmelt storm events (WRCC, 2022; NRCS, 2022; Table 1)
 469 but their runout varied in terms of erosion rate, grain size (Figure 6b), depositional behavior (Figure 6c) and the
 470 topographic convergence of the underlying terrain.

471 **Table 1.** Landslide and runout characteristics

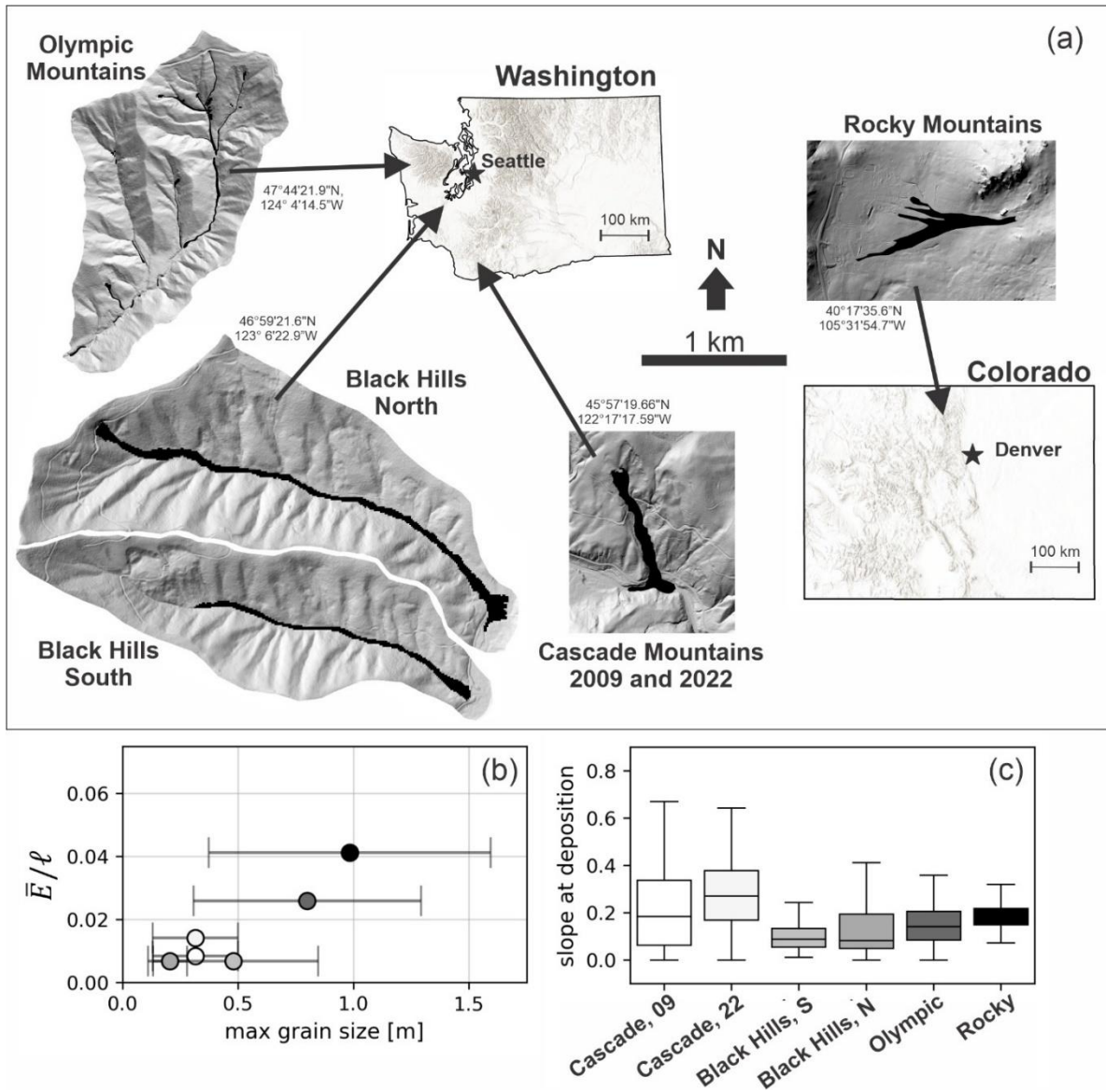
site	Cascade Mountains, 09	Cascade Mountains, 22	Black Hills, south	Black Hills, north	Rocky Mountains	Olympic Mountains
initial landslide body length [m]	185	55	80	75	40	45
initial landslide body width [m]	80	50	15	65	35	15
initial landslide body volume [m ³]	110,000	22,000	1,500	18,500	4,600	400 - 2,200
2-day cumulative precipitation + snowmelt [mm]	120+85	140+75	205+50	205+50	193+0	100 - 220 + ?
maximum grain size [m]	0.316	0.316	0.48	0.206	0.984	0.8
slope range of positive-net deposition [%]	1 - 15	1 - 15	<1 - 10	<1 - 8	16 - 25	5 - 15
average flow depth in scour zone [m] ^a	4	2	2	3	3	3
average channel slope in scour zone [m/m]	0.25	0.25	0.15	0.15	0.4	0.3
average channel width in scour zone [m]	45	20	25	35	55	10
length of erosion, [m]	600	340	1210	1345	360	2550
erosion area, A [m ²]	28,400	6,600	22,800	52,400	20,800	28,900
erosion volume, $\sum E\Delta x^2$ [m ³] ^b	44,547	5,125	12,332	26,815	34,275	33,725
average erosion per unit length of runout debris, \bar{E}/ℓ , [m/m]	0.0085	0.014	0.0068	0.0068	0.041	0.026
k	0.020	0.034	0.017	0.020	0.076	0.051
growth factor, [m ³ /m]	74.2	15.1	10.2	19.9	95.2	13.2
average observed $ \Delta\eta $ [m]	2.4	2.2	0.53	0.63	0.89	1.4
total erosion volume / total mobilized volume ^c	0.29	0.19	0.89	0.59	0.88	0.97

472 ^a rough approximation based on landslide volume, channel width and height of scour marks in erosion zone

473 ^b excludes landslide volume

474 ^c total mobilized volume = initial landslide body + erosion volume

475



476

477 **Figure 6** (a) Landslide locations in Washington and Colorado states. Coordinates next to each site are WGS84.
 478 Shaded DEMs of each site are shown at the same scale. (b) Observed average erosion rate per unit landslide length
 479 (\bar{E}/ℓ) relative to the observed average-maximum grainsize. Error bars indicate standard deviation. (c) Underlying
 480 topographic slope of observed deposition.

481 5.2 Model setup and field parameterization

482 Each model was set up on a 10-meter grid representation of the pre-event DEM. The extent of the initial mass wasting
 483 source material (e.g., the initial landslide body) was interpreted from a combination of lidar, air-photo and field
 484 observations. At all locations, we use Equation (13) to approximate shear stress. We field-surveyed each site, noting
 485 the maximum flow thickness, typical deposition and erosion depths and the size of the largest grains in the runout
 486 deposits.

487 We estimated parameter values from these field and remote observations (See Table 1). A site-specific value for k
488 was determined as a function of the observed average erosion depth (determined as total erosion volume divided by
489 the erosion area, \bar{E}) relative to the length of the runout debris, which we approximated as the length of the initial
490 landslide body (ℓ). Further details are described in the Appendix.

491 The volume of the initial landslide body ranged in volume from 400 to 110,000 m³ across sites. At all sites, erosion
492 and subsequent entrainment added to the total mobilized volume (initial landslide body + erosion volume), but the
493 contribution was highly variable. The erosion volume divided by the total mobilized volume was as low as 0.19 at the
494 Cascade Mountain, 2022 landslide to as high as 0.97 at the Olympic Mountain landslides (Table 1).

495 The average maximum grain size varied from 0.2 m at the Black hills sites to nearly 1 m at the Rocky Mountain Site
496 (Figure 6b, Table 1). Values of \bar{E}/ℓ ranged from 0.007 to 0.041 [m/m] with the highest rate occurring at the Rocky
497 Mountain landslide and the lowest at the Black Hills sites. Details on grain-size samples and data collected in the field
498 are described in the Supplementary Material. In terms of growth factors (average volumetric erosion per unit length
499 of the erosion-dominated region of the runout path, Hungr et al. 1984; Reid et al., 2016) values ranged from 10 m³/m
500 at the Black Hills South site to 95 m³/m during the Rocky Mountain landslide (Table 1).

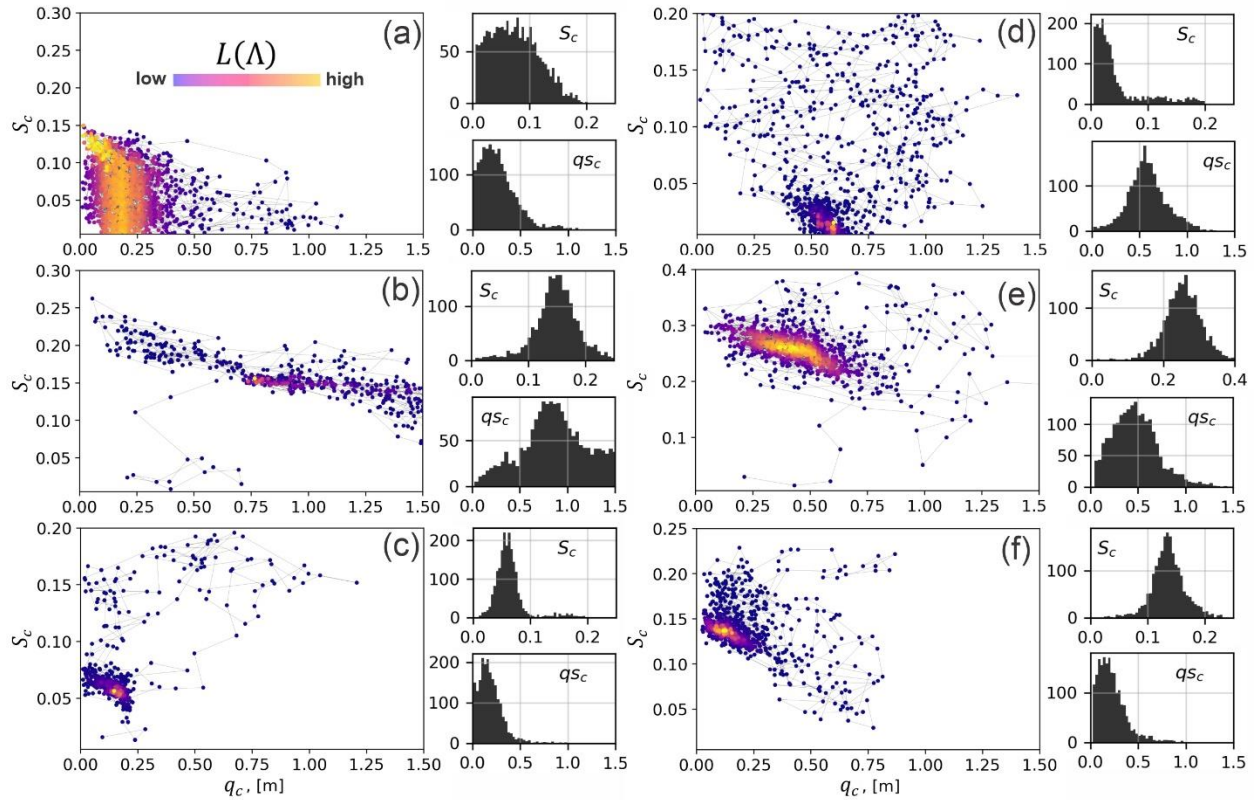
501 The median values of topographic slopes at which observed deposition occurred (i.e., $\Delta\eta > 0$) ranged between 0.1
502 and 0.3 across sites, while deposition was also observed in much steeper (>0.4) slopes, and much flatter slopes at some
503 sites (Figure 6c) (Table 1). The slope of channel reaches where net deposition (cumulative erosion and deposition;
504 e.g., Guthrie et al., 2010) was positive tended to be lowest at the Black Hills site (<1% to 10%) and highest at Rocky
505 Mountain site (16% to 25%).

506 We defined uniform prior distributions of S_c and q_c and then used the calibration utility to find the best-fit parameter
507 values (parameter values corresponding to the highest $L(\Lambda)$). Minimum and maximum values of S_c were initially
508 estimated from the range of observed slope of areas of positive-net deposition (Table 1). Minimum and maximum
509 values of q_c were set as 0.01 to 1.75, which roughly represents the range of minimum observed thickness of debris
510 flow termini in the field at all of the validation sites. For the purpose of implementing the calibration utility, we
511 prepared a DoD of each site. The DoD was determined either from repeated lidar or field observations as detailed in
512 the Supplementary Material.

513 **5.3 Calibration and model performance**

514 Markov chains, colored according to the likelihood index, $L(\Lambda)$ are plotted in the S_c - q_c domain, along with
515 histograms of sampled S_c and q_c values for each landslide in Figure 7. Each Markov chain includes 2000 model
516 iterations. The runtime for 2000 model iterations depended on model domain, landslide size and number of landslides
517 modeled but varied from roughly 1.5 for the Cascade, 2022 landslide to 6 hours for the Olympic Mountain landslides
518 on a 2016 2.1 GHz Intel Core Xeon, 32 GB memory desktop. The chains show a wide array of sampling patterns and
519 parameter ranges but broadly speaking, at all sites, the algorithm jumped within S_c - q_c space towards higher $L(\Lambda)$, to
520 form bell-shaped posterior distributions for each parameter. Depending on the landslide type, the calibration algorithm
521 converged on different S_c - q_c pairs. For example, at the Cascade Mountains site, the calibration utility converged to
522 smaller q_c and S_c values for the 2009 event (Figure 7a), which permitted thinner flows over lower slopes and

523 effectively made the 2009 modelled runout more mobile relative to the 2022 modelled runout (Figure 7b). At the
 524 Rocky Mountains site (Figure 7e), a relatively high q_c value helps control lateral extent of the modelled runout that in
 525 the field was controlled by standing trees (see Supplementary Material).



526
 527 **Figure 7.** MWR calibration results for (a) Cascade Mountains, 2009; (b) Cascade Mountains, 2022, (c) Black Hills,
 528 South; (d) Black Hills, North; (e) Rocky Mountains and; (f) Olympic Mountains. Each result shows a scatter plot of
 529 the sampled S_c and q_c values, colored by their relative $L(\Lambda)$ value. Note y-axis scale differs between plots. To the
 530 right of each scatter plot are histograms of the iterated S_c and q_c parameters, which can be normalized to represent
 531 an empirical PDF of the possible S_c and q_c values that calibrate MWR to the site. Histogram y-axis is count and x-
 532 axis is S_c or q_c , as indicated on the histogram.

533
 534 Profile plots of modelled Q_s and maps of the modelled planimetric runout extent, colored to indicate where the runout
 535 matched (α), overestimated (β) or underestimated (γ) the observed runout are shown in Figure 8. Values of Ω_T we
 536 obtained with MWR are comparable or higher than reported values of Ω_T in the literature that used a variety of models
 537 (Gorr et al., 2022; Barnhart et al., 2021; Note, to compare Ω_T values to those studies, subtract 1 from values reported
 538 in this study). Across the sites, the volumetric error of the model, $\Delta\eta_E$, ranges between 6% and 15% (median 9.1%)
 539 of the total mobilized volume from the observed DoD. An overall <10% volumetric error is reasonable considering
 540 the low number of parameters required to calibrate MWR and that empirical estimates of total mobilized volume used
 541 to run other runout models can vary by as much of an order of magnitude (e.g., Gartner et al., 2014; Barnhart et al.,
 542 2021). Model performance in predicting volume flux along the runout profile was within similar error ranges. Except
 543 for the Rocky Mountains site where MWR consistently modelled wider-than-observed flow, the cumulative flow error

544 along the runout profile (Q_{sE}) were limited to 5%-19% of the mean cumulative flow determined from the observed
545 DoD.

546 MWR generally successfully replicates observed sediment transport along the runout path via model parameterizations
547 that are unique to each landslide. For example, the profile plots of Q_s at the Cascade Mountain site (Figure 8a and 8b)
548 show that during the 2009 landslide, all of the runout material flowed past the first 750 meters of the runout path.
549 During the 2022 landslide, material began to deposit just down slope of the initial landslide scar, as both observed and
550 modelled Q_s reverse slope, indicating loss in downstream volume flux. Model comparisons in the Cascade Mountains
551 site were limited to the upper 750 m of the hillslope because a large portion of the runout material was lost to fluvial
552 erosion in the valley (see Supplementary Material).

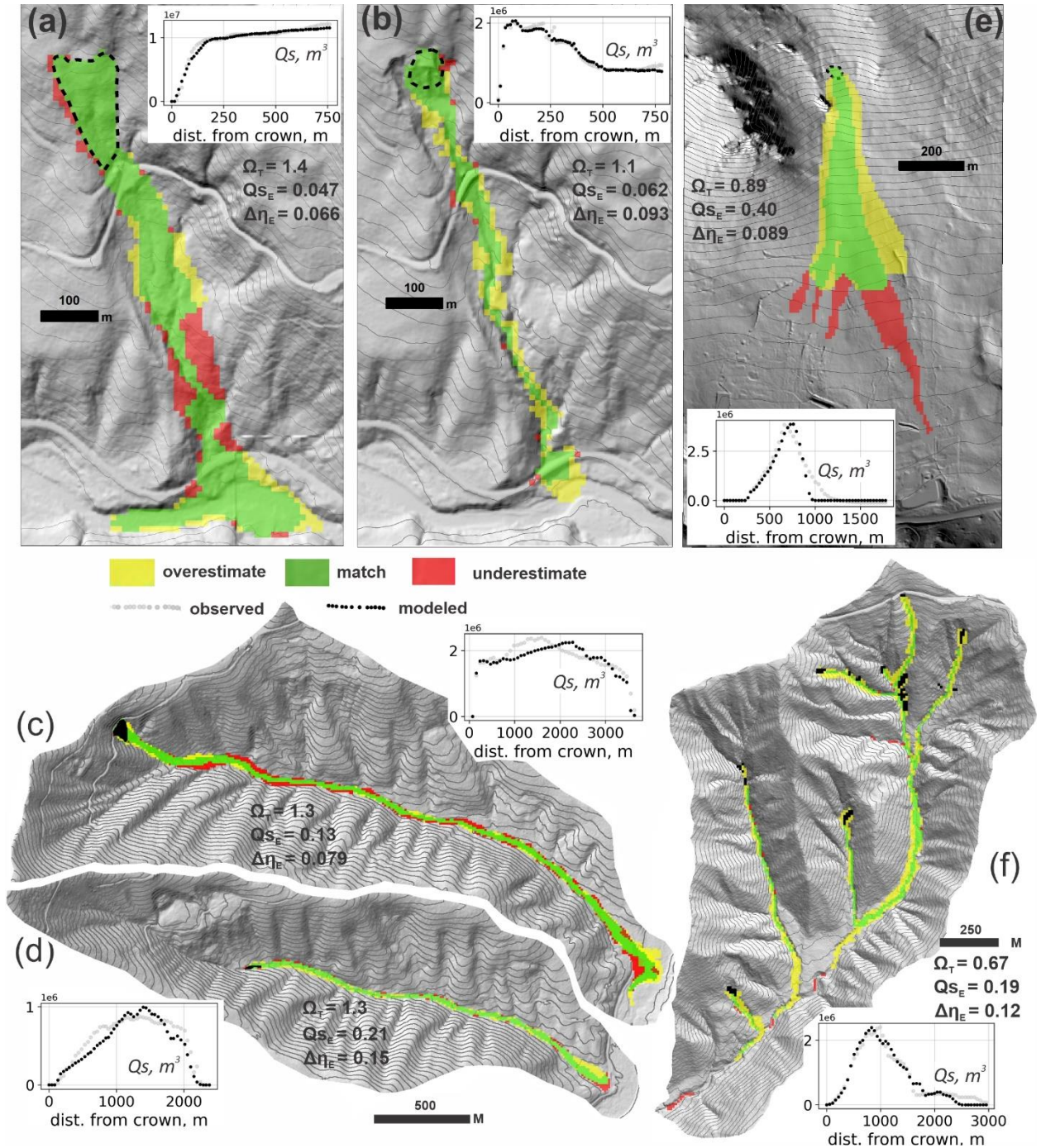
553 MWR also successfully replicates the observed sediment transport patterns at the Olympic Mountains site (profile plot
554 of Q_s in Figure 8f) and to a lesser degree, the Rocky Mountain site (Figure 8e). This finding is notable, because at the
555 Olympic Mountain site, observed runout extent and sediment depositional pattern were heavily impacted by woody
556 debris. Similarly, at the Rocky Mountains site, the width of the runout appeared to be restricted by trees. (See
557 Supplementary Material).

558 Using a fixed cell size of 10-m might have impacted model performance in some areas. MWR tended to over-estimate
559 the runout width for small landslides like the Olympic Mountains and Cascade Mountains, 2022 sites (yellow zones
560 in Figures 8f and 8b), likely because of the 10-m grid size used to represent the terrain. A 10-m DEM is generally
561 accepted as a good balance between model detail and computational limitations (e.g., Horton et al. 2013). However,
562 for small landslides, the 10-m grid is close to the size of the channels that controlled observed runout (Supplementary
563 Material) and may not have accurately represented the terrain. Modelled flow was less topographically-constrained
564 and tended to flow over a wider area of the terrain than observed in the more confined and smaller channels within
565 the axis of the runout valleys.

566 Because MWR does not have an explicit representation of flow momentum, it may show poor performance in regions
567 of the runout path where flow momentum is the primary control on runout extent. For example, at the Cascade
568 Mountain, 2009 slide, MWR underestimates the slope-perpendicular flow over a bench (large red zone in Figure 8a).
569 Review of model behavior for this slide (Figure 9) shows how MWR successfully mimics diverging flow around a
570 broad ridge upslope of the bench (iteration $t=28$ in Figure 9), but afterwards continues to follow topographic slope
571 and converges too rapidly into a narrow ravine along the west edge of the bench (iteration $t=40$ in Figure 9; compare
572 to runout scar in air photo and underestimated region on topographic bench in Figure 8a). At the Rocky Mountains
573 site, in addition to standing trees, the forward momentum of the runout may have also restricted lateral spread of the
574 observed runout. Modelled runout is consistently too wide.

575 Overall, calibration was best at the Cascade Mountain, 2009 landslide (values of Ω_T are highest and values of $\Delta\eta_E$
576 and Q_{sE} are lowest) and poorest at the Rocky Mountain and Olympic Mountain sites (Values of Ω_T are lowest Q_{sE}
577 and $\Delta\eta_E$ are highest). At both the Rocky Mountain and Olympic Mountain sites, because we lacked repeat lidar, we
578 created the DoD from a map of field estimated erosion and deposition depths and estimated the pre-event DEM. The
579 lower calibration scores may indicate that field estimated DoDs were not as accurate as those determined via lidar
580 differencing. Another source of uncertainty that we have not addressed in our study is regolith thickness. Using

581 spatially accurate regolith thickness, rather than a uniform thickness, would likely improve MWR performance too.
 582 Nonetheless, although imperfect, at most sites, MWR does not appear to have a strong systematic bias in modeled
 583 output, which suggests that MWR may not have any structural weaknesses; however the consistent over-estimated
 584 width on planar to divergent topography at the Rocky Mountain site requires further investigation at similar sites to
 585 determine if this issue is due to calibration or the model.



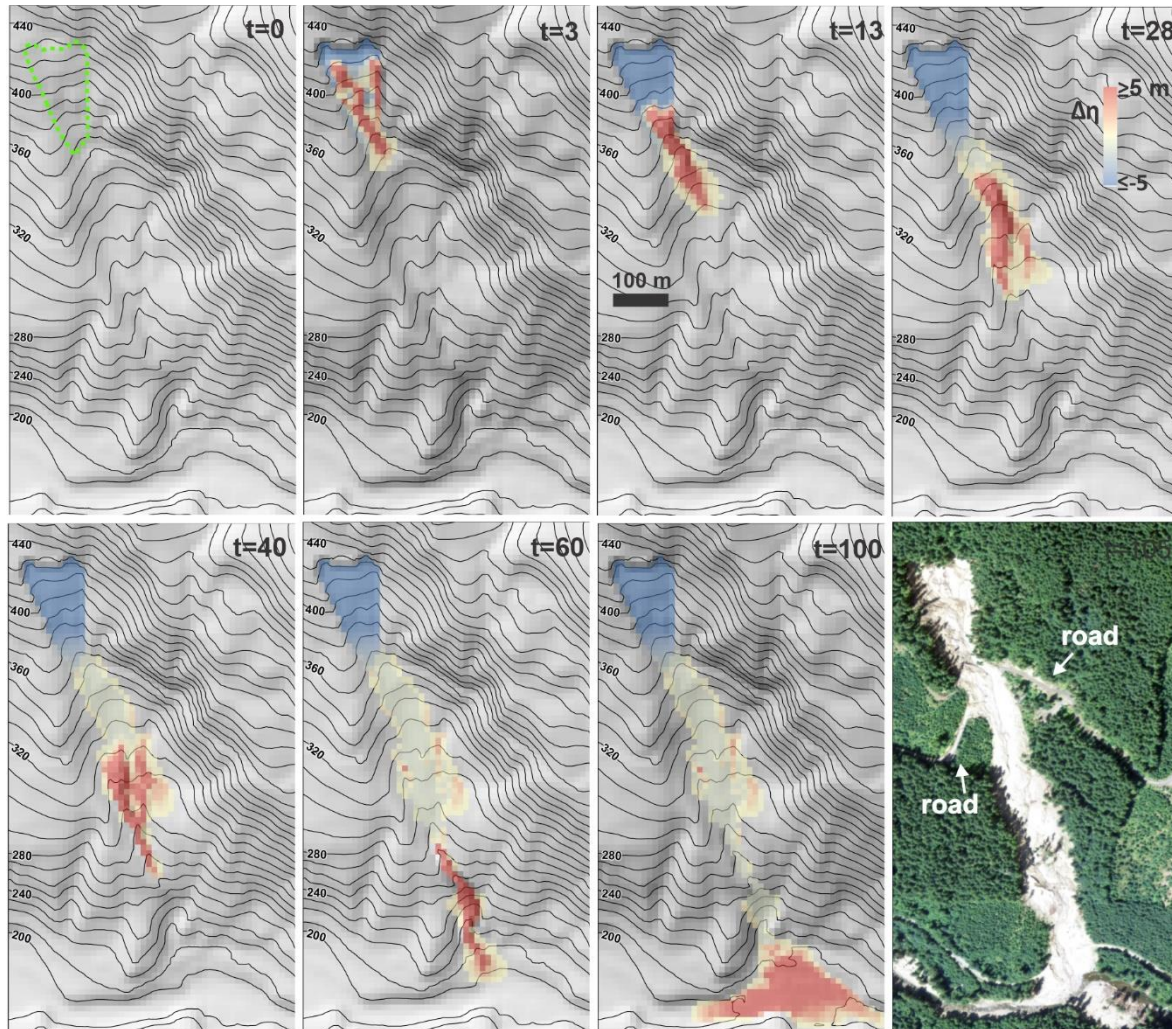
586
 587 **Figure 8.** Calibrated model performance as indicated by maps of modeled runout extent, profile plots of observed
 588 and modeled cumulative sediment transport along the centerline of the runout path (Q_s , see equation 28) and

589 reported values of Ω_T , $\Delta\eta_E$ and Q_{SE} . Y-axis label for profile plots of Q_s indicated on plot. In all maps, up is north
 590 except in (e), north is towards the left. (a) Cascade Mountains, 2009; (b) Cascade Mountains, 2022; (c) Black Hills,
 591 North; (d) Black Hills, South; (e) Rocky Mountains; (f) Olympic Mountains.

592

593

594



595

596 **Figure 9.** Illustration of modeled runout of the Cascade Mountains, 2009 landslide beginning from the initial
 597 movement of the landslide body to final deposition in the river valley that demonstrates MWR response to
 598 topography. Note how the landslide slip surface directs the initial flow. Topography lines reflect the underlying
 599 terrain, which is updated after each iteration. Air photo in last panel shows observed runout extent. Note that upper
 600 road is not part of the observed landslide runout path.

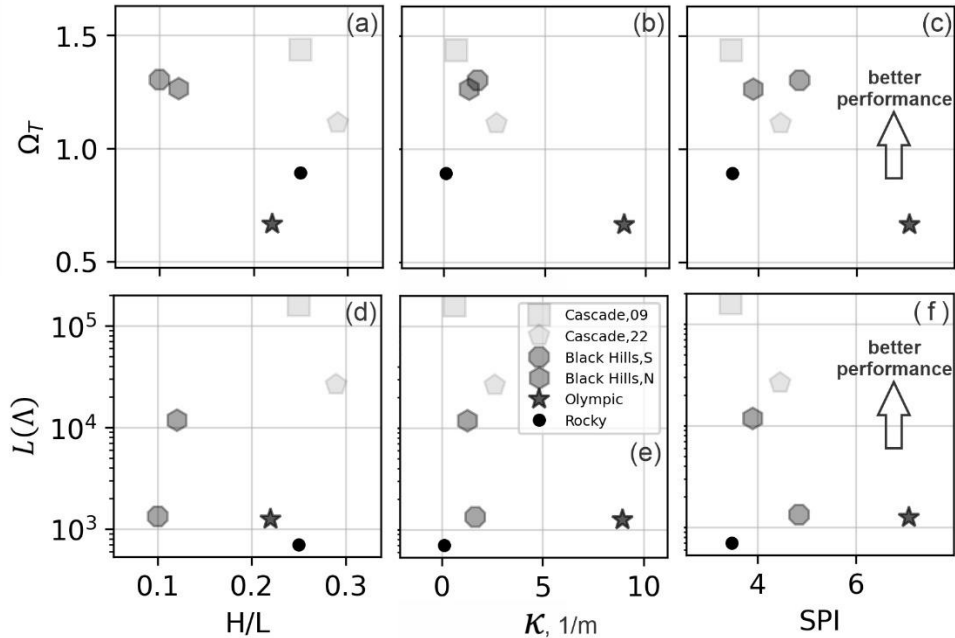
601 To understand whether the ability to calibrate MWR systematically varies with topography of the runout path, we
 602 compared model performance with three topographic indices described by Chen & Yu (2011). The indices are
 603 computed from the terrain in the observed runout extent and include the relief ratio (H/L), mean total curvature (κ)
 604 and the mean specific stream power index (SPI). The index H/L equals the average slope of the runout path (or

605 relative relief), determined as the total topographic relief of the runout (measured from the center of the landslide to
606 the end of the runout path) divided by the horizontal length of the runout and indicates the mobility of the runout.
607 Index κ represents topographic convergence, which is the second derivative of the terrain surface, with increasingly
608 positive values of index κ reflecting growing topographic convergence and concave-up channel profile (e.g.,
609 Istanbuloglu et al., 2008). The index SPI is determined as the natural log of the product of the contributing area and
610 slope. Indices κ and SPI are computed at each node in the runout extent and model performance is compared to the
611 mean value.

612 Comparison of model performance with respect to the topographic indices in Figure 10 shows: slightly improved
613 model performance over runout paths that are less convergent (lower SPI and κ values) and on steeper terrain (higher
614 H/L) but neither trend is significant. The latter finding appears to be mostly a result of how well modelled sediment
615 transport and topographic change (Q_{sE} and $\Delta\eta_E$) replicated observed, as there does not appear to be a trend in Ω_T with
616 H/L and the two best performing models (both Cascade Mountain landslides) had the lowest (best) Q_{sE} values and
617 low $\Delta\eta_E$ values. Both findings are likely impacted by the grid size we used to represent terrain. As noted above, at all
618 sites we used a 10-m grid, but at some sites 10-m doesn't quite capture the relief of channelized topography that
619 controlled observed runout, leading to modelled runout that was considerably wider than observed and causing low
620 Ω_T value (this is especially true at the Olympic Mountains site, Figure 10a, b and c). Also, it is important to note that
621 these indices were calculated for the extent of the observed debris flows and may not represent the topographic form
622 that controlled the model.

623 In summary, using the calibration utility, we showed how MWR can be calibrated to a range of different landslide
624 types and runout terrains. To a certain degree, though calibration, MWR can be parameterized to compensate for
625 deficiencies in the DEM or processes not explicitly represented in the model (momentum, woody debris). A
626 relationship between model performance and topography was not eminent. This finding is likely a result of the
627 contributions of numerous factors other than the terrain form, such as the DEM resolution, the quality of the DoD and
628 importance of processes not explicitly included in the model that also impact performance.

629



630
 631 **Figure 10.** Illustration of model calibration, as reflected by the posterior parameter likelihood $L(\theta)$ and planimetric
 632 fit (Ω_T) relative to topographic indices. There is no strong trend between the topographic indices and calibration
 633 performance. Note, curvature values are scaled by a factor of 100.

634 **6. Discussion**

635 **6.1 Strategic testing of MWR for hazard mapping applications**

636 Having demonstrated basic model response to topography and that MWR can be calibrated to a variety of landslides
 637 and runout terrains, we now strategically test MWR using the Cascade Mountain and Black Hills sites. Since both of
 638 these sites include two separate landslides, we can thus test model performance by swapping best-fit model parameters
 639 at each site, rerunning the models and comparing results with the original, calibrated results. At the Cascade Mountain
 640 site, the 2009 and 2022 landslides originated on the same hillslope (Figure 8a and 8b). At Black Hills site, the two
 641 landslides occurred on different hillslopes but in adjacent east-west oriented watersheds (Figure 8c and 8d).

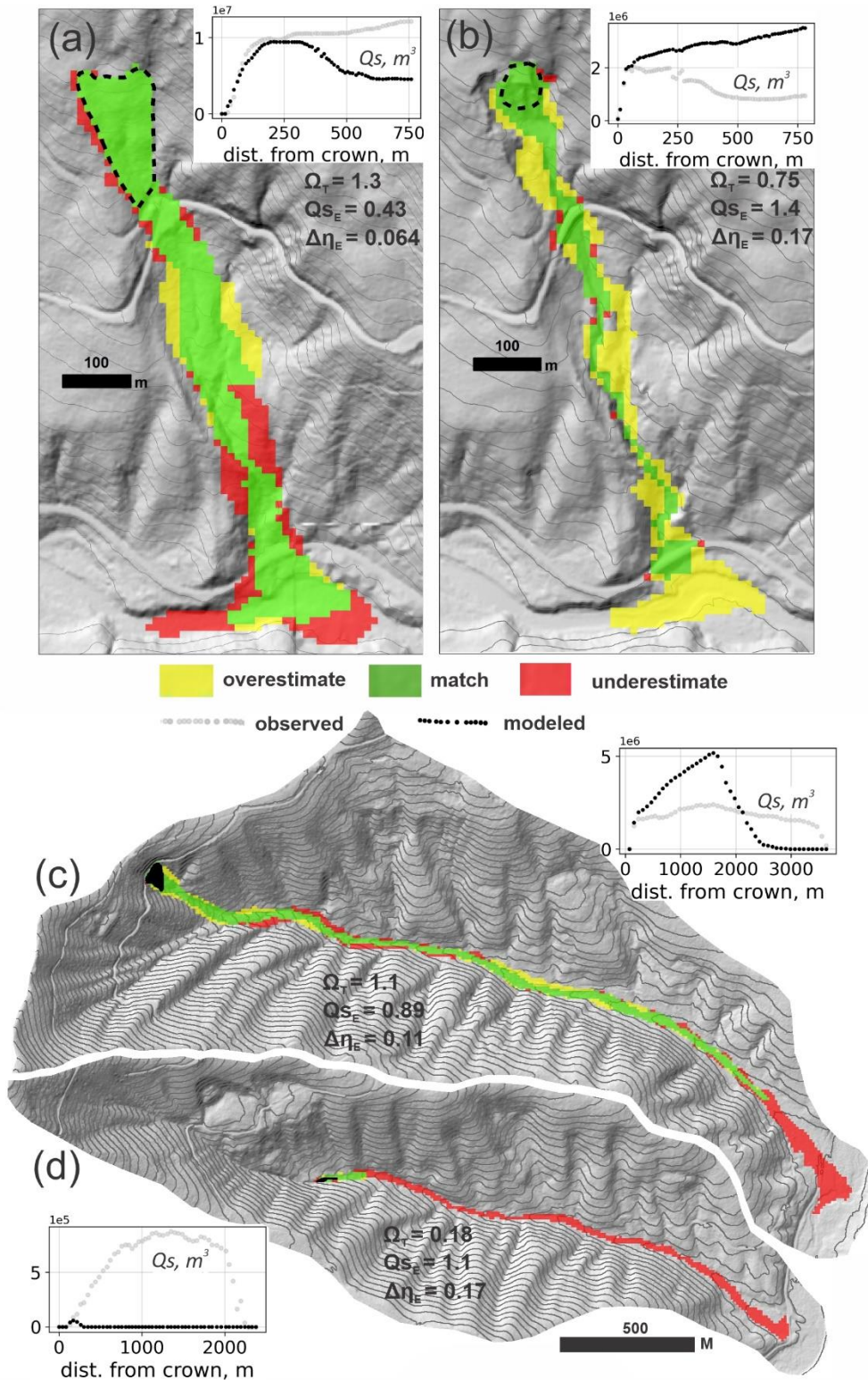
642 As shown in Figure 11, at three of the landslides (both Cascade Mountain landslides and the Black Hills, North
 643 landslide), when the best-fit parameters from the other landslide are used to predict runout, the accuracy of modelled
 644 runout planimetric extent drops but resultant Ω_T values can still be as high or higher than values reported in other
 645 studies (compare to equivalent Ω_T values in Gorr et al., 2022 and Barnhart et al., 2021). In terms of modelled sediment
 646 transport and topographic change, swapping best-fit parameters has a more substantial effect. At the Cascade
 647 Mountain, 2009 landslide, using the 2022 best-fit parameter values causes about half of the modelled runout material
 648 to prematurely deposit on the hillslope, reducing the amount of sediment that reaches the valley floor (Q_{SE} increases
 649 by a factor of nine; Figure 11). Using the Cascade Mountain, 2009 parameter values on the Cascade Mountain, 2022
 650 landslide (Figure 11b) increases modelled runout extent and results in nearly four times the entrainment and transport
 651 of sediment to the valley floor, causing Q_{SE} to increase by a factor of 20 and $\Delta\eta_E$ by 83%. At the Black Hills site,

652 using the South basin best-fit model parameters at the North basin causes Q_{sE} and $\Delta\eta_E$ increase by 83% and 39%
653 respectively (Figure 11c). Unlike the other three landslides, swapping best-fit parameters at the Black Hills, South
654 landslide results in both large sediment transport and runout extent error because the North basin best-fit parameters
655 cause modelled landslide to entrain too little and stop only a few hundred meters from the initial source area (Figure
656 11d).

657 Although the need for calibration of MWR is a limitation for its transferability across sites, this limitation holds true
658 for most physics-based models. Barnhart et al. (2021) compared the ability of three different detailed-mechanistic
659 models to replicate an observed post-wildfire debris-flow runout event in California, USA. All three models used a
660 shallow-water-equation-based approach that conserved both mass and momentum, representing the flow as either a
661 single phase or double phase fluid. All models gave comparable results in simulating the event, suggesting that there
662 may not be a “true” best model. Despite the high level of detail and processes explicitly included in each model, all
663 models were sensitive to and required an estimate of the total mobilized volume, and the ability to replicate observed
664 runout ultimately depended on calibration of the parameters used to characterize debris flow properties.

665

666

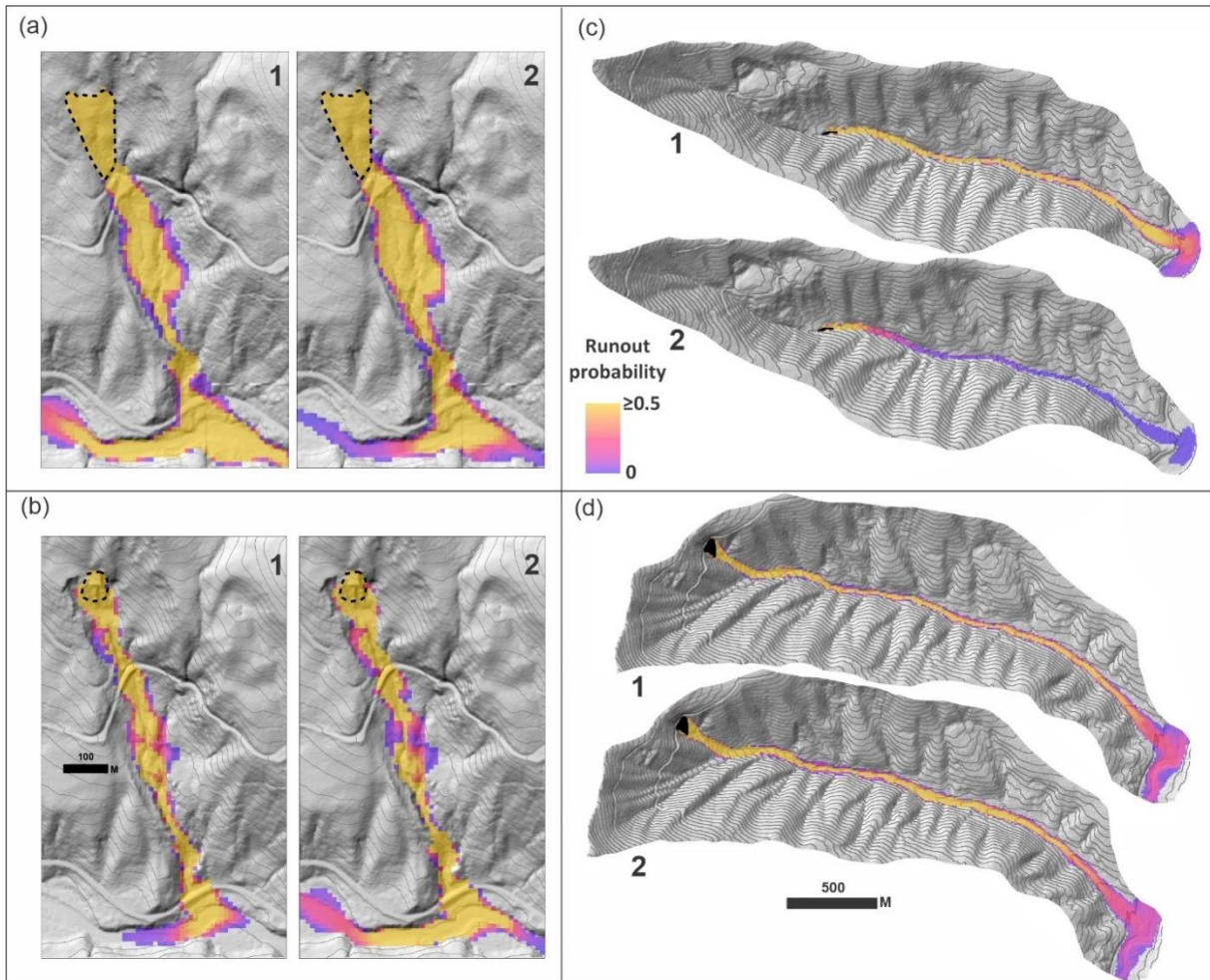


667

668 **Figure 11.** Model performance using the neighboring landslide parameter values, as indicated by modeled runoff
 669 extent, profile plots of Q_s , reported values of Ω_T , $\Delta\eta_E$ and Q_{s_E} . Compare with Figure 8. (a) Cascade Mountain,
 670 2009; (b) Cascade Mountain, 2022; (c) Black Hills, North; (d) Black Hills, South

671
672
673
674
675
676
677
678

As landslide hazard models often forecast hazard probabilistically, an alternative test to simply swapping the best-fit parameters is to swap parameter PDFs determined from the calibration utility and compare probability of runout at each model node (equation 30). As shown in Figure 12, similar to the first test, at three of the landslides, using the parameter distribution associated with the neighbouring landslide results in relatively minor changes in whether runout is likely to occur versus not occur (probability of runout $\geq 50\%$; Figures 12a, 12b and 12d). At the Black Hills South landslide, swapping parameter PDFs causes a large change in runout probability (Figure 12c).



679
680
681
682
683
684
685
686
687
688

Figure 12. Model tests by swapping parameter PDFs and comparing runout probability at the (a) Cascade Mountain, 2009; (b) Cascade Mountain, 2022; (c) Black Hills, South and; (d) Black Hills, North sites. (1) runout using parameter distributions of the site and (2) runout using parameter distributions of the neighboring site.

The results of these two tests suggest that site-specific calibration may be needed when the user aims to apply MWR to sediment budget analyses; however, we suspect that this finding is a consequence of testing the model at a site with very different landslide types and runout processes. At sites like the Cascade Mountain and Black Hills sites, which consisted of a diverse range of landslide processes including small, confined debris flows to large, unconfined debris avalanches, MWR may need to be calibrated to each type of landslide and predictive applications might involve

689 applying the appropriate parameter set based on landslide type. In regions where landslide processes are relatively
690 uniform (like the Olympic Mountain site), calibration to one landslide might be sufficient to predict the depositional
691 patterns and sediment transport at another. Finally, as noted in Section 3.1, we found numerous parameter
692 combinations allowed MWR to match observed runout extent. This finding suggests that if the project aim is limited
693 to an evaluation of runout extent, model calibration to the site may not be as critical and parameter values from
694 calibration to nearby landslides or even globally-available repeated DEMs and airphotos that show the slope of past
695 landslide deposits (for S_c) and how thick their frontal lobes are at the point of deposition (for q_c), might be sufficient.

696 **6.2. MassWastingRunout probability applications**

697 In this section we briefly demonstrate how to determine runout probability from a probabilistically determined
698 landslide hazard map or a specific, potentially unstable slope using MWR. The first application may be appropriate
699 for watershed- to regional-scale runout hazard assessments. The second application is an example hazard assessment
700 for a potentially unstable hillslope. Both applications are demonstrated at the Olympic Mountain site where landslide
701 size and type tended to be relatively uniform and parameter PDFs determined through calibration may therefore
702 represent typical runout processes in the basin.

703 **6.2.1. Runout probability from a landslide hazard map**

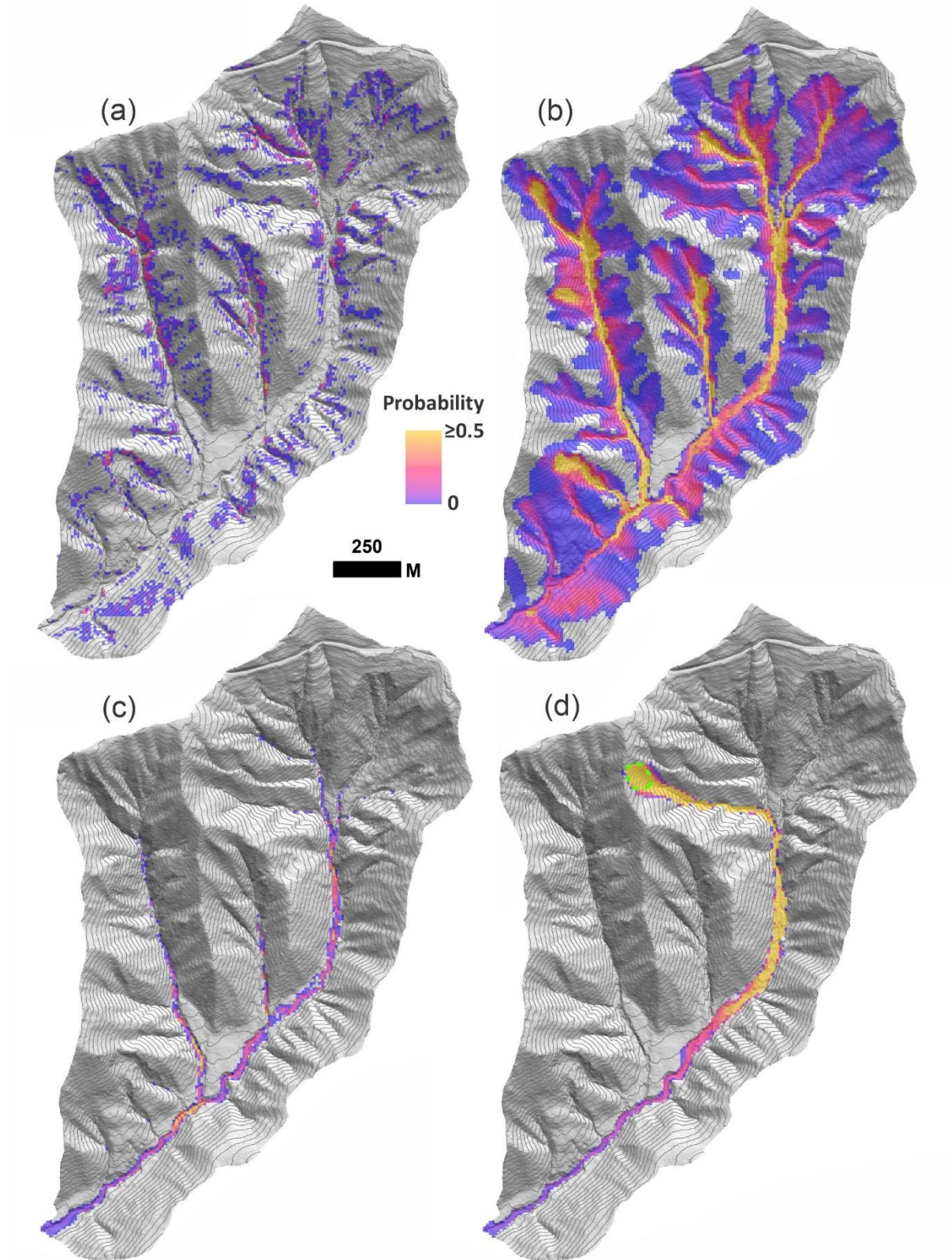
704 To determine runout probability from a landslide hazard map, we ran MWR Probability using Option 3, reading a
705 series of mapped landslide source areas created by an externally run Monte Carlo landslide initiation model. For the
706 landslide initiation model, we used LandslideProbability, an existing component in Landlab that computes landslide
707 probability by iteratively calculating Factor-of-Safety (FS : ratio of the resisting to the driving forces) at each node on
708 the raster model grid Np times from randomly selected soil (regolith) hydrology properties (e.g., soil depth, saturated
709 hydraulic conductivity) soil strength (friction angle, cohesion) and recharge rates (precipitation input rate minus
710 evapotranspiration and soil storage). Landslide probability at a node is defined as the number of times $FS < 1$ divided
711 by Np .

712 We first ran LandslideProbability using a 50-year precipitation event (WRCC, 2017) to determine landslide
713 probability (Figure 13a) over the entire Olympic Mountains model domain and create the series of Np FS maps.
714 Details on the LandslideProbability setup are included in the Supplementary Material. We then read the series of FS
715 maps into MWR Probability, treating all nodes with $FS < 1$ as a landslide source, and ran MWR Np times. Each
716 iteration, MWR read a new FS map and randomly selected a new set of parameter values from S_c - q_c parameter PDFs
717 created by the calibration utility.

718 Runout probability results are illustrated in Figure 13b and show that the probability of runout is high in many of the
719 second order channels but low at the basin outlet. As discussed in Section 3, the probability of aggradation or erosion
720 caused by the runout can also be determined by adjusting the numerator of Eq. (30) and the probability of deposition
721 greater than 1 meter is shown in Figure 13c. In this example, in addition to MWR parameter uncertainty, runout
722 probability reflects uncertainty in landslide size and location caused by a 50-year precipitation event.

723 **6.2.2 Runout probability for a specific, potentially unstable slope**

724 When field evidence or other data indicate that a specific hillslope may be potentially unstable, but the exact area of
725 a potential landslide on that slope is unknown, MWR can be used to generate a hazard estimate that takes into account
726 the uncertainty in the landslide area. For this application, MWR Probability is run using Option (2), which requires a
727 polygon representing the extent of the potentially unstable slope. We designated a 0.6 ha, convergent hillslope in the
728 headwaters of the Olympic Mountains site as a potentially unstable slope (Figure 13d). For each model repetition, a
729 landslide area can form anywhere within the potentially unstable slope and is at least as large as a user defined
730 minimum size but no larger than the potentially unstable slope. This example shows that, given uncertainty in the
731 landslide size and location, and uncertainty in MWR parameterization, if a landslide were to initiate on the potentially
732 unstable slope, the probability of the runout reaching the basin outlet is less than 5%.



733
734
735
736

Figure 13. Olympic Mountain site: (a) Landslide probability, $P(FS \leq 1)$. (b) Corresponding runout probability, $P(\Delta\eta)$. (c) Probability of deposition greater than 1 m and (d) Runout probability for the potentially unstable slope (green-dashed polygon).

737 7.0 Concluding remarks

738 In this study, we described, calibrated and tested MassWastingRunout (MWR), a new cellular-automaton landslide
739 runout model that combines the functionality of simple runout algorithms used in landscape evolution and watershed
740 sediment yield models (WSMs) with the predictive detail typical of runout models used for landslide inundation hazard
741 mapping. MWR is implemented in Python as a component for the Landlab earth surface modelling toolkit and is
742 designed for probabilistic landslide hazard assessments, sediment transport and landscape evolution applications.
743 MWR includes a Markov Chain Monte Carlo calibration utility that determines the best-fit parameter values for a site
744 as well as empirical Probability Density Functions (PDF) of the parameter values. MWR also includes a utility called
745 MWR Probability that takes the PDF output from the calibration utility to determine runout probability.

746 Results indicate that despite its simple conceptualization, MWR shows skill in modeling the final runout extent,
747 sediment transport and topographic change associated with a landslide. MWR needs only the location and geometry
748 of an initial landslide source area to model the entire runout process. When compared to other models capable of
749 replicating observed landslide inundation patterns, the strength of MWR lies in its use of field-inferable parameters,
750 its ability to internally estimate the total mobilized volume (initial landslide body + erosion volume) and its relatively
751 parsimonious model design.

752 MWR can be calibrated to a site using just two parameters (critical slope, S_c , and a threshold flux for deposition, q_c)
753 and the MWR calibration utility enables the user to calibrate the model for a watershed within several hours on a
754 standard desktop (Section 5.3). Although the predictive power of MWR hinges on calibration—a common requirement
755 for mechanistic models—its reliance on two calibration parameters serves to constrain model uncertainty. Site-specific
756 calibration may be needed when MWR is used for sediment budget analysis, but if the aim is limited to mapping
757 runout extent, it may be possible to infer parameterization from nearby landslides or possibly from globally available
758 repeated DEMs and air photos that show where past mass-wasting flows have stopped (for S_c) and how thick their
759 frontal lobes are at the point of deposition (for q_c). Nonetheless, as a rules-based, cellular-automaton model, MWR is
760 not designed to accurately simulate flow depth. For accurate flow depths or debris flow impact forces, a detailed-
761 mechanistic modeling approach should be used.

762 MWR shows a rich set of intuitive responses to topographic curvature and slope. When calibrated to the runout of six
763 different observed landslides, the volumetric error of MWR, $\Delta\eta_E$, ranged between 6% and 15% (median 9.1%) of the
764 observed total mobilized volume. Except for the Rocky Mountains site where MWR consistently modelled wider-
765 than-observed flow, the cumulative flow error along the runout profile (Q_{sE}) were limited to 5%-19% of the mean
766 cumulative flow determined from the observed DEM-of-Difference (DoD). These are considered acceptable levels of
767 performance given that the total mobilized volume of many debris flow models assume an order of magnitude range
768 of confidence. A notable finding of this paper is that MWR modeled runout did not have any strong systematic bias
769 in predictions (toward unrealistically short or wide flows, for example), which suggests that MWR is structurally
770 sound. However, MWR may underperform compared to mechanistic models when flow momentum is the primary
771 driver of runout extent. (e.g., in areas of slope-perpendicular flow).

772 As a component of the Landlab earth surface modelling toolkit, MWR is designed to be compatible with other models.
773 MWR can be readily coupled with a landslide initiation model (e.g., LandslideProbability) and geomorphic transport

774 laws for hillslope diffusion and fluvial incision to investigate the role of landslides and their runout on long-term
 775 landscape evolution. In this study we showed how to couple MWR with LandslideProbability to map debris flow
 776 hazard when landslide initiation location is uncertain. Future studies will explore large-scale application in landscape
 777 evolution or sediment yield models, and characterize model parameters for different geologic and hydroclimatic
 778 conditions. The use of a calibrated runout model in WSMs might allow for region-specific and more insightful
 779 predictions of landslide impact on landscape morphology and watershed-scale sediment dynamics.

780

781 **Appendix A - Determination of k**

782 The average erosion depth caused by the observed runout (\bar{E}) can be determined from the DoD as the total erosion
 783 volume ($\sum E \Delta x^2$) divided by the erosion area (\mathbb{A}) in the DoD:

$$784 \quad \bar{E} = \frac{\sum E \Delta x^2}{\mathbb{A}} \quad (\text{A1})$$

785 where $\sum E \Delta x^2$ and \mathbb{A} exclude the initial landslide body volume and area, areas of deposition ($\Delta \eta > 0$) and areas
 786 with no change in elevation ($\Delta \eta = 0$). In terms of the debris flow conceptualization used in MWR, \bar{E} can also be
 787 written as a function of the mean number of times a debris flow would need to pass over a grid cell (\bar{n}) multiplied by an
 788 average erosion depth per debris flow (\bar{h}_e) to equal \bar{E} as:

$$789 \quad \bar{E} = \bar{n} \bar{h}_e \quad (\text{A2})$$

790 An estimate for \bar{n} can be determined from the average length of the runout material, which we approximate simply
 791 as the mapped landslide length (ℓ) divided by the cell width:

$$792 \quad \bar{n} = \frac{\ell}{\Delta x} \quad (\text{A3})$$

793 Note that if the observed runout formed as a result of multiple landslides (as was the case at the Olympic Mountain
 794 site, see Supplementary Material), then ℓ was determined as the sum of the initial landslide body lengths. Also, as
 795 the debris flows move down slopes in excess of S_c , they entrain material, split, and spread, and the runout material
 796 tends to lengthen. Using the initial landslide length to represent the runout length thus represents a minimum value
 797 for \bar{n} and if needed, (A2) can be multiplied by a coefficient to scale ℓ into a more representative runout length.

798 Combining (A2) and (A3), \bar{h}_e can be defined as the average erosion rate per unit length of runout debris (\bar{E}/ℓ) times
 799 the cell width:

$$800 \quad \bar{h}_e = \frac{\bar{E} \Delta x}{\ell} \quad (\text{A4})$$

801 Rewriting equation (11) as a function of the average shear stress in the erosion-dominated reaches of the runout path
 802 ($\bar{\tau}$) and assuming $\tau_c \cong 0$, debris flow erodibility parameter k can be estimated as:

$$803 \quad k = \frac{\bar{h}_e}{\bar{\tau}} \quad (\text{A5})$$

804 To solve for k , we estimated $\bar{\tau}$ from field-approximated debris flow depth and channel slope measurements in the
805 erosion-dominated reaches of the runout path. To estimate flow depth, we used the height of scour marks on the
806 channel wall or tree trunks, above the channel bed (Table 1). We used (13) to define $\bar{\tau}$. For D_s , we used the average
807 maximum grain size observed over the whole runout path. If τ is defined as a function of grain-collision dependent
808 shear stress approach (13) and k is determined as a function of f , as in (A5), the impact of f on model behavior is
809 relatively small.

810 Notation

811	q_{R_i}	[m]	debris flux from a node to each of the node i -th receiver nodes
812	q_O	[m]	the total out-going debris flux
813	Nr		the number of receiving nodes of node n
814	S_i		the underlying topographic slope ($\tan \theta$) to each of the node i -th receiver nodes
815	a		exponent in (1) that controls how flow is distributed to downslope nodes
816	q_I	[m]	The total incoming flux
817	Nd		number of donors nodes to a node
818	q_{D_j}	[m]	the flux from node D_j (the j -th donor node)
819	h	[m]	flow depth at node, adjusted to be no more than h_{max}
820	h_{max}	[m]	the maximum observed flow depth
821	A	[m]	aggradation depth
822	S_c		critical slope
823	S		steepest slope to the node's eight neighbouring nodes
824	Δx	[m]	cell length
825	$A_{p N_a}$	[m]	potential aggradation depth that forms a deposit that spreads over N_a consecutive nodes
826	$A_{p,i}$	[m]	i -th deposition amount in the deposit illustrated in Figure 4
827	N_a		number of nodes qs_n^I is assumed to spreads over
828	E	[m]	erosion depth
829	h_r	[m]	regolith depth
830	h_e	[m]	potential erosion depth
831	θ	[°]	topographic slope used to determine shear stress, equal to $\tan^{-1}(S)$
832	τ	[Pa]	basal shear stress
833	τ_c	[Pa]	critical shear stress of the regolith
834	k		erodibility parameter in (11)
835	f		exponent, controls the non-linearity of h_e in (11)
836	ρ	[kg/m ³]	density of runout material
837	σ	[Pa]	normal stress at basal surface
838	φ		tangent of collision angle between grains, measured from the vertical axis
839	v_s		volumetric solids concentration
840	ρ_s	[kg/m ³]	density of solids
841	D_s	[m]	characteristic particle diameter
842	u	[m/s]	depth average flow velocity
843	z	[m]	depth below the flow surface
844	u^*		shear velocity
845	g	[m/s]	acceleration due to gravity
846	$\Delta\eta$	[m]	change in elevation at node
847	\mathbf{q}_D		a vector containing all q_{D_j} sent to the node
848	ξ_D		a vector containing the incoming attribute values for each q_{D_j}
849	ξ_D		attribute value delivered to the node
850	ξ_R		attribute value sent to receiver nodes

851	ξ		attribute value at node
852	η	[m]	topographic elevation
853	Λ		parameter set
854	$L(\Lambda)$		likelihood of parameter set
855	$p(\Lambda)$		prior probability of parameter set
856	Ω_T		the Lee-Salle index for evaluating model planimetric fit
857	α	[m ²]	modelled area of matching extent (compared to observed runout extent)
858	β	[m ²]	modelled area of overestimated extent
859	γ	[m ²]	modelled area of underestimated extent
860	$\Delta\eta_E$		volumetric error of the modelled topographic change relative to the observed total
861			mobilized volume, fraction.
862	V	[m ³]	observed total mobilized volume
863	p		the number of nodes in the modelled runout extent
864	$\Delta\eta_{Mi}$	[m]	the modelled topographic change [m] at the i -th node within the runout extent
865	$\Delta\eta_{Oi}$	[m]	the observed topographic change [m] at the i -th node within the runout extent
866			
867	Q_{sE}		mean-modelled-cumulative flow error along the runout path relative to the observed
868			mean cumulative flow, fraction.
869	j		index used to represent each node along a profile of the runout path.
870	$\Delta\eta_{ij}$	[m]	topographic change [m] at the i -th node located upstream of node j
871	u_j		total number of all nodes located upstream of node j
872	r		the number of nodes along the center line of the runout path
873	Q_s	[m ³]	the cumulative debris flow volume at each node, j along the center line of the runout path
874	Q_{sO}	[m ³]	the observed cumulative debris flow volume (Q_s) at each node, j
875	Q_{sM}	[m ³]	the modeled cumulative debris flow volume (Q_s) at each node, j
876	$\Delta\eta_{ij}$	[m]	the topographic change [m] at the i -th node located upstream of node j
877	u_j		the total number of all nodes located upstream of j
878	\overline{Q}_{sO}	[m ³]	the observed mean cumulative flow
879	$P(\Delta\eta)$		
880	\overline{E}/ℓ	[m/m]	average erosion per unit length of runout debris
881	$P(\Delta\eta)$		probability of runout, expressed as the probability that the elevation of a node changes
882	#		number of
883	Np		number Monte Carlo iterations used to determine probability
884	A	[m ²]	erosion area of the observed or modeled runout
885	\overline{E}	[m]	average erosion depth caused by the runout
886	$\sum E\Delta x^2$	[m ³]	the total erosion volume
887	\bar{n}		mean number of times a debriton would need to pass over a grid cell multiplied by an
888			average erosion depth per debriton to equal \overline{E}
889	\bar{h}_e	[m]	average erosion depth per debriton
890	ℓ	[m]	length of runout debris, approximated as the length of the initial landslide body
891	H/L		the total topographic relief of the runout (measured from the center of the landslide to the
892			end of the runout path) divided by the horizontal length of the runout
893	κ	[1/m]	mean total curvature
894	SPI		mean specific stream power index
895	FS		Factor-of-Safety, ratio of the resisting to the driving forces acting on a hillslope
896			

897 **Code availability**

898 MassWastingRunout and several tutorial notebooks area available at: <https://github.com/landlab/landlab>

899 **Acknowledgements**

900 This research was partially supported by the following programs: National Science Foundation (NSF)
901 PREEVENTS program, ICER-1663859; NSF OAC-2103632; and NASA Grant number 22-RRNES22-
902 0010 and benefited from critical referee reviews. Stephen Slaughter field reviewed the Cascade
903 Mountains, 2009 and Black Hills landslides the year they occurred and provided photos and field
904 observations that aided author interpretation. John Jenkins helped with the 2022 field reconnaissance the
905 Cascade Mountains landslide. Eli Schwat helped with field reconnaissance at the Olympic Mountains site.
906 This work also benefitted from Landlab support and coding guidance from Eric Hutton and helpful
907 feedback from many others.

908 **Competing interests**

909 The contact author has declared that none of the authors has any competing interests.

910

911 **References**

912 Bagnold, R. A.: Experiments on a gravity-free dispersion of large solid spheres in a Newtonian fluid under shear.
913 Proceedings of the Royal Society of London, 225(1160), 49–63. <https://doi.org/10.1098/rspa.1954.0186>, 1954.

914 Barca, D., Crisci, G., Di Gregorio, S., and Nicoletta, F.: Cellular automata method for modelling lava flows:
915 Simulation of the 1986–1987 eruption, Mount Etna, Sicily, in Kilburn, C., and Luongo, G., eds., Active lavas:
916 Monitoring and modeling: London, University College of London Press, p. 291–309, 1993.

917 Barnhart, K. R., Hutton, E. W. H., Tucker, G. E., Gasparini, N. M., Istanbuluoglu, E., Hopley, D. E. J., Lyons, N. J.,
918 Mouchene, M., Nudurupati, S. S., Adams, J. M., & Bandaragoda, C.: Short communication: Landlab v2.0: a software
919 package for Earth surface dynamics. *Earth Surface Dynamics*, 8(2), 379–397. [https://doi.org/10.5194/esurf-8-379-](https://doi.org/10.5194/esurf-8-379-2020)
920 [2020](https://doi.org/10.5194/esurf-8-379-2020), 2020.

921 Barnhart, K. R., Jones, R., George, D. J., McArdell, B. W., Rengers, F. K., Staley, D. M., & Kean, J. W.: Multi-Model
922 Comparison of Computed Debris Flow Runout for the 9 January 2018 Montecito, California Post-Wildfire Event.
923 *Journal of Geophysical Research: Earth Surface*, 126(12). <https://doi.org/10.1029/2021jf006245>, 2021.

924 Benda, L., & Dunne, T.: Stochastic forcing of sediment supply to channel networks from landsliding and debris flow.
925 *Water Resources Research*, 33(12), 2849–2863. <https://doi.org/10.1029/97wr02388>, 1997.

926 Benda, L., Veldhuisen, C. P., & Black, J.: Debris flows as agents of morphological heterogeneity at low-order
927 confluences, Olympic Mountains, Washington. *Geological Society of America Bulletin*, 115(9), 1110.
928 <https://doi.org/10.1130/b25265.1>, 2003.

929 Beven, K.: A manifesto for the equifinality thesis. *Journal of Hydrology*, 320(1–2), 18–36.
930 <https://doi.org/10.1016/j.jhydrol.2005.07.007>, 2006.

931 Burton, A., & Bathurst, J. C.: Physically based modelling of shallow landslide sediment yield at a catchment scale.
932 *Environmental Geology*, 35(2–3), 89–99. <https://doi.org/10.1007/s002540050296>, 1998.

933 Bigelow, P., Benda, L., Miller, D., & Burnett, K. M.: On Debris Flows, River Networks, and the Spatial Structure of
934 Channel Morphology. *Forest Science*, 53(2), 220–238. <https://doi.org/10.1093/forestscience/53.2.220>, 2007

935 Campforts, B., Shobe, C. M., Overeem, I., & Tucker, G. E.: The Art of Landslides: How Stochastic Mass Wasting
936 Shapes Topography and Influences Landscape Dynamics. *Journal of Geophysical Research: Earth Surface*, 127(8).
937 <https://doi.org/10.1029/2022jf006745>, 2022

938 Campforts, B., Shobe, C. M., Steer, P., Vanmaercke, M., Lague, D., & Braun, J.: HyLands 1.0: a hybrid landscape
939 evolution model to simulate the impact of landslides and landslide-derived sediment on landscape evolution.
940 *Geoscientific Model Development*, 13(9), 3863–3886. <https://doi.org/10.5194/gmd-13-3863-2020>, 2020.

941 Capart, H., & Fraccarollo, L.: Transport layer structure in intense bed-load. *Geophysical Research Letters*, 38(20),
942 n/a. <https://doi.org/10.1029/2011gl049408>, 2011.

943 Capart, H., Hung, C., & Stark, C. R.: Depth-integrated equations for entraining granular flows in narrow channels.
944 *Journal of Fluid Mechanics*, 765. <https://doi.org/10.1017/jfm.2014.713>, 2015.

945 Carretier, S., Martinod, P., Reich, M., & Godd ris, Y.: Modelling sediment clasts transport during landscape evolution.
946 *Earth Surface Dynamics*, 4(1), 237–251. <https://doi.org/10.5194/esurf-4-237-2016>, 2016.

947 Chase, C. G.: Fluvial landsculpting and the fractal dimension of topography. *Geomorphology*, 5(1–2), 39–57.
948 [https://doi.org/10.1016/0169-555x\(92\)90057-u](https://doi.org/10.1016/0169-555x(92)90057-u), 1992.

949 Chen, C., & Yu, F.: Morphometric analysis of debris flows and their source areas using GIS. *Geomorphology*, 129(3–
950 4), 387–397. <https://doi.org/10.1016/j.geomorph.2011.03.002>, 2011.

951 Chen, H., & Zhang, L.: EDDA 1.0: integrated simulation of debris flow erosion, deposition and property changes.
952 *Geoscientific Model Development*, 8(3), 829–844. <https://doi.org/10.5194/gmd-8-829-2015>, 2015.

953 Chen, T.-Y. K., Wu, Y.-C., Hung, C.-Y., Capart, H., and Voller, V. R.: A control volume finite-element model for
954 predicting the morphology of cohesive-frictional debris flow deposits, *Earth Surface Dynamics*, 11, 325–342,
955 <https://doi.org/10.5194/esurf-11-325-2023>, 2023.

956 Clerici, A., & Perego, S.: Simulation of the Parma River blockage by the Corniglio landslide (Northern Italy).
957 *Geomorphology*, 33(1–2), 1–23. [https://doi.org/10.1016/s0169-555x\(99\)00095-1](https://doi.org/10.1016/s0169-555x(99)00095-1), 2000.

958 Codd, E. F.: *Cellular Automata* (1st ed.). New York, Academic Press, 1968.

959 Coz, J. L., Renard, B., Bonnifait, L., Branger, F., & Boursicaud, R. L.: Combining hydraulic knowledge and uncertain
960 gaugings in the estimation of hydrometric rating curves: A Bayesian approach. *Journal of Hydrology*, 509, 573–587.
961 <https://doi.org/10.1016/j.jhydrol.2013.11.016>, 2014.

962 Crave, A., & Davy, P.: A stochastic “precipiton” model for simulating erosion/sedimentation dynamics. *Computers*
963 *& Geosciences*, 27(7), 815–827. [https://doi.org/10.1016/s0098-3004\(00\)00167-9](https://doi.org/10.1016/s0098-3004(00)00167-9), 2001.

964 D’Ambrosio, D., Di Gregorio, S., Iovine, G., Lupiano, V., Rongo, R., & Spataro, W.: First simulations of the Sarno
965 debris flows through Cellular Automata modelling. *Geomorphology*, 54(1–2), 91–117. [https://doi.org/10.1016/s0169-555x\(03\)00058-8](https://doi.org/10.1016/s0169-555x(03)00058-8), 2003.

967 Egashira, S., Honda, N., & Itoh, T.: Experimental study on the entrainment of bed material into debris flow. *Physics*
968 *and Chemistry of the Earth, Parts a/B/C*, 26(9), 645–650. [https://doi.org/10.1016/s1464-1917\(01\)00062-9](https://doi.org/10.1016/s1464-1917(01)00062-9), 2001.

969 Foglia, L., Hill, M. C., Mehl, S. W., and Burlando, P. (2009), Sensitivity analysis, calibration, and testing of a
970 distributed hydrological model using error-based weighting and one objective function, *Water Resources*
971 *Research*, 45, W06427, doi:10.1029/2008WR007255.

972 Fannin, R. J., & Wise, M. P.: An empirical-statistical model for debris flow travel distance. *Canadian Geotechnical*
973 *Journal*, 38(5), 982–994. <https://doi.org/10.1139/t01-030>, 2001.

974 Frank, F., McArdell, B. W., Huggel, C., & Vieli, A.: The importance of entrainment and bulking on debris flow runout
975 modeling: examples from the Swiss Alps. *Natural Hazards and Earth System Sciences*, 15(11), 2569–2583.
976 <https://doi.org/10.5194/nhess-15-2569-2015>, 2015.

977 Freeman, T. G.: Calculating catchment area with divergent flow based on a regular grid. *Computers &*
978 *Geosciences*, 17(3), 413–422. [https://doi.org/10.1016/0098-3004\(91\)90048-j](https://doi.org/10.1016/0098-3004(91)90048-j), 1991.

979 Gartner, J. E., Cannon, S. H., & Santi, P. M.: Empirical models for predicting volumes of sediment deposited by debris
980 flows and sediment-laden floods in the transverse ranges of southern California. *Engineering Geology*, 176, 45–56.
981 <https://doi.org/10.1016/j.enggeo.2014.04.008>, 2014.

982 Gelman, A., Carlin, J. B., Stern, H. S., Dunson, D. B., Vehtari, A., & Rubin, D. B.: *Bayesian Data Analysis* (3rd ed.).
983 Electronic Edition, 2021.

984 Goode, J. R., Luce, C. H., & Buffington, J. M.: Enhanced sediment delivery in a changing climate in semi-arid
985 mountain basins: Implications for water resource management and aquatic habitat in the northern Rocky Mountains.
986 *Geomorphology*, 139–140, 1–15. <https://doi.org/10.1016/j.geomorph.2011.06.021>, 2012.

987 Gorr, A., McGuire, L. A., Youberg, A., & Rengers, F. K.: A progressive flow-routing model for rapid assessment of
988 debris-flow inundation. *Landslides*, 19(9), 2055–2073. <https://doi.org/10.1007/s10346-022-01890-y>, 2022

989 Guthrie, R., Hockin, A., Colquhoun, L., Nagy, T., Evans, S. G., & Ayles, C. P.: An examination of controls on debris
990 flow mobility: Evidence from coastal British Columbia. *Geomorphology*, 114(4), 601–613.
991 <https://doi.org/10.1016/j.geomorph.2009.09.021>, 2010.

992 Guthrie, R. H., & Befus, A. D.: DebrisFlow Predictor: an agent-based runout program for shallow landslides. *Natural*
993 *Hazards and Earth System Sciences*, 21(3), 1029–1049. <https://doi.org/10.5194/nhess-21-1029-2021>, 2021.

994 Hammond C.J., Prellwitz R.W., Miller S.M.: Landslides hazard assessment using Monte Carlo simulation. In: Bell
995 DH (ed) Proceedings of 6th international symposium on landslides, Christchurch, New Zealand, Balkema, vol 2. pp
996 251–294, 1992.

997 Han, Z., Chen, G., Li, Y., Tang, C., Xu, L., He, Y., Huang, X., & Wang, W.: Numerical simulation of debris-flow
998 behavior incorporating a dynamic method for estimating the entrainment. *Engineering Geology*, 190, 52–64.
999 <https://doi.org/10.1016/j.enggeo.2015.02.009>, 2015.

1000 Han, Z., Li, Y., Huang, J., Chen, G., Xu, L., Tang, C. Y., Zhang, H., & Shang, Y.: Numerical simulation for run-out
1001 extent of debris flows using an improved cellular automaton model. *Bulletin of Engineering Geology and the
1002 Environment*, 76(3), 961–974. <https://doi.org/10.1007/s10064-016-0902-6>, 2017.

1003 Han, Z., Ma, Y., Li, Y., Zhang, H., Chen, N., Hu, G., & Chen, G.: Hydrodynamic and topography based cellular
1004 automaton model for simulating debris flow run-out extent and entrainment behavior. *Water Research*, 193, 116872.
1005 <https://doi.org/10.1016/j.watres.2021.116872>, 2021.

1006 Heiser, M., Scheidl, C., & Kaitna, R.: Evaluation concepts to compare observed and simulated deposition areas of
1007 mass movements. *Computational Geosciences*, 21(3), 335–343. <https://doi.org/10.1007/s10596-016-9609-9>, 2017.

1008 Hobley, D. E. J., Adams, J. M., Nudurupati, S. S., Hutton, E. W. H., Gasparini, N. M., Istanbuloglu, E., & Tucker,
1009 G. E.: Creative computing with Landlab: an open-source toolkit for building, coupling, and exploring two-dimensional
1010 numerical models of Earth-surface dynamics. *Earth Surface Dynamics*, 5(1), 21–46. [https://doi.org/10.5194/esurf-5-
1011 21-2017](https://doi.org/10.5194/esurf-5-21-2017), 2017.

1012 Holmgren, P.: Multiple flow direction algorithms for runoff modelling in grid based elevation models: An empirical
1013 evaluation. *Hydrological Processes*, 8(4), 327–334. <https://doi.org/10.1002/hyp.3360080405>, 1994

1014 Horton, P., Jaboyedoff, M., Rudaz, B., & Zimmermann, M. N.: Flow-R, a model for susceptibility mapping of debris
1015 flows and other gravitational hazards at a regional scale. *Natural Hazards and Earth System Sciences*, 13(4), 869–885.
1016 <https://doi.org/10.5194/nhess-13-869-2013>, 2013.

1017 Hungr, O., Morgan, G. J., & Kellerhals, R.: Quantitative analysis of debris torrent hazards for design of remedial
1018 measures. *Canadian Geotechnical Journal*, 21(4), 663–677. <https://doi.org/10.1139/t84-073>, 1984.

1019 Hungr, O., & Evans, S. G.: Entrainment of debris in rock avalanches: An analysis of a long run-out mechanism.
1020 *Geological Society of America Bulletin*, 116(9), 1240. <https://doi.org/10.1130/b25362.1>, 2004.

1021 Hutter, K., Svendsen, B., & Rickenmann, D.: Debris flow modeling: A review. *Continuum Mechanics and
1022 Thermodynamics*, 8(1), 1–35. <https://doi.org/10.1007/bf01175749>, 1996.

1023 Iovine, G., D’Ambrosio, D., & Di Gregorio, S.: Applying genetic algorithms for calibrating a hexagonal cellular
1024 automata model for the simulation of debris flows characterised by strong inertial effects. *Geomorphology*, 66(1–4),
1025 287–303. <https://doi.org/10.1016/j.geomorph.2004.09.017>, 2005.

1026 Istanbuluoglu, E. Bras R. L.: Vegetation-modulated landscape evolution: Effects of vegetation on landscape
1027 processes, drainage density, and topography. *Journal of Geophysical Research*, 110(F2).
1028 <https://doi.org/10.1029/2004jf000249>, 2005.

1029 Istanbuluoglu, E., Bras R. L., Flores-Cervantes, H., and Tucker, G. E.: Implications of bank failures and fluvial
1030 erosion for gully development: Field observations and modeling, *J. Geophysical Research*, 110, F01014,
1031 doi:10.1029/2004JF000145, 2005.

1032 Istanbuluoglu, E., O. Yetemen, E. R. Vivoni, H. A. Gutie´rrez-Jurado, and R. L. Bras, Eco-geomorphic implications
1033 of hillslope aspect: Inferences from analysis of landscape morphology in central New Mexico, *Geophysical. Research*
1034 *Letters*, 35, L14403, 10.1029/ 2008GL034477, 2008.

1035 Iverson, R. M.: The physics of debris flows. *Reviews of Geophysics*, 35(3), 245–296.
1036 <https://doi.org/10.1029/97rg00426>, 1997.

1037 Iverson, R. M., & Denlinger, R. P.: Flow of variably fluidized granular masses across three-dimensional terrain: 1.
1038 Coulomb mixture theory. *Journal of Geophysical Research*, 106(B1), 537–552.
1039 <https://doi.org/10.1029/2000jb900329>, 2001.

1040 Iverson, R.M., How should mathematical models of geomorphic processes be judged?. In Wilcock, P., & Iverson, R.
1041 (Eds.), *Prediction in Geomorphology*. American Geophysical Union, 2003.

1042 Julien, P. Y., & Paris, A.: Mean Velocity of Mudflows and Debris Flows. *Journal of Hydraulic Engineering*, 136(9),
1043 676–679. [https://doi.org/10.1061/\(asce\)hy.1943-7900.0000224](https://doi.org/10.1061/(asce)hy.1943-7900.0000224), 2010.

1044 Kean, J. W., Staley, D. M., Lancaster, J., Rengers, F., Swanson, B., Coe, J., et al.: Inundation, flow dynamics, and
1045 damage in the 9 January 2018 Montecito debris-flow event, California, USA: Opportunities and challenges for post-
1046 wildfire risk assessment. *Geosphere*, 15(4), 1140–1163. <https://doi.org/10.1130/GES02048.1>, 2019

1047 Korup, O.: Effects of large deep-seated landslides on hillslope morphology, western Southern Alps, New Zealand.
1048 *Journal of Geophysical Research*, 111(F1). <https://doi.org/10.1029/2004jf000242>, 2006

1049 Lancaster, S. T., Hayes, S. K., & Grant, G. E.: Effects of wood on debris flow runout in small mountain watersheds.
1050 *Water Resources Research*, 39(6). <https://doi.org/10.1029/2001wr001227>, 2003.

1051 Larsen, I. J., & Montgomery, D. R.: Landslide erosion coupled to tectonics and river incision. *Nature Geoscience*,
1052 5(7), 468–473. <https://doi.org/10.1038/ngeo1479>, 2012.

1053 Liu, J., Wu, Y., Gao, X., & Zhang, X.: A Simple Method of Mapping Landslides Runout Zones Considering Kinematic
1054 Uncertainties. *Remote Sensing*, 14(3), 668. <https://doi.org/10.3390/rs14030668>, 2022.

1055 Major, J. J.: Depositional Processes in Large-Scale Debris-Flow Experiments. *The Journal of Geology*, 105(3), 345–
1056 366. <https://doi.org/10.1086/515930>, 1997.

1057 Major, J. J., & Iverson, R. M.: Debris-flow deposition: Effects of pore-fluid pressure and friction concentrated at flow
1058 margins. *Geological Society of America Bulletin*, 111(10), 1424–1434. [https://doi.org/10.1130/0016-7606\(1999\)111,](https://doi.org/10.1130/0016-7606(1999)111)
1059 1999.

1060 McCoy, S. W., Kean, J. W., Coe, J. A., Tucker, G. S., Staley, D. M., & Wasklewicz, T. A.: Sediment entrainment by
1061 debris flows: In situ measurements from the headwaters of a steep catchment. *Journal of Geophysical Research*,
1062 117(F3), n/a. <https://doi.org/10.1029/2011jf002278>, 2012.

1063 McDougall, S., & Hungr, O.: A model for the analysis of rapid landslide motion across three-dimensional terrain.
1064 *Canadian Geotechnical Journal*, 41(6), 1084–1097. <https://doi.org/10.1139/t04-052>, 2004.

1065 Medina, V., Hürlimann, M., & Bateman, A.: Application of FLATModel, a 2D finite volume code, to debris flows in
1066 the northeastern part of the Iberian Peninsula. *Landslides*, 5(1), 127–142. [https://doi.org/10.1007/s10346-007-0102-](https://doi.org/10.1007/s10346-007-0102-3)
1067 [3](https://doi.org/10.1007/s10346-007-0102-3), 2008.

1068 Montgomery, D. R., & Dietrich, W. E.: Where do channels begin? *Nature*, 336(6196), 232–234.
1069 <https://doi.org/10.1038/336232a0>, 1988.

1070 Murray, B.A., & Paola, C.: A cellular model of braided rivers. *Nature*, 371(6492), 54–57.
1071 <https://doi.org/10.1038/371054a0>, 1994.

1072 Murray, A. B., & Paola, C.: Properties of a cellular braided-stream model. *Earth Surface Processes and Landforms*,
1073 22(11), 1001–1025. [https://doi.org/10.1002/\(sici\)1096-9837\(199711\)22:11](https://doi.org/10.1002/(sici)1096-9837(199711)22:11), 1997.

1074 Murray A.B.: Which Models Are Good (Enough), and When?. In: John F. Shroder (ed.) *Treatise on Geomorphology*,
1075 Volume 2, pp. 50-58. San Diego: Academic Press, 2013.

1076 Natural Resources Conservation Service | Snow and Water Interactive Map (n.d.). Natural Resources Conservation
1077 Service. <https://www.nrcs.usda.gov/resources/data-and-reports/snow-and-water-interactive-map>, Accessed April,
1078 2022

1079 Nudurupati, S. S., Istanbuluoglu, E., Tucker, G. E., Gasparini, N. M., Hobley, D. E. J., Hutton, E. W. H., Barnhart,
1080 K. R., & Adams, J. M.: On transient semi-arid ecosystem dynamics using Landlab: vegetation shifts, topographic
1081 refugia, and response to climate. *Water Resources Research*, 59(4). <https://doi.org/10.1029/2021wr031179>, 2023.

1082 Perron, J. T.: Climate and the Pace of Erosional Landscape Evolution. *Annual Review of Earth and Planetary Sciences*,
1083 45(1), 561–591. <https://doi.org/10.1146/annurev-earth-060614-105405>, 2017.

1084 Reid, M. J., Coe, J. A., & Brien, D. L.: Forecasting inundation from debris flows that grow volumetrically during
1085 travel, with application to the Oregon Coast Range, USA. *Geomorphology*, 273, 396–411.
1086 <https://doi.org/10.1016/j.geomorph.2016.07.039>, 2016.

1087 Renard, B., Garreta, V., & Lang, M. J.: An application of Bayesian analysis and Markov chain Monte Carlo methods
1088 to the estimation of a regional trend in annual maxima. *Water Resources Research*, 42(12).
1089 <https://doi.org/10.1029/2005wr004591>, 2006.

1090 Rengers, F. K., McGuire, L. A., Kean, J. W., Staley, D. M., and Hobley, D. E. J.: Model simulations of flood and
1091 debris flow timing in steep catchments after wildfire, *Water Resources Research*, 52, 6041–6061,
1092 doi:10.1002/2015WR018176, 2016.

1093 Roda-Boluda, D. C., D'Arcy, M., McDonald, J., & Whittaker, A. C.: Lithological controls on hillslope sediment
1094 supply: insights from landslide activity and grain size distributions. *Earth Surface Processes and Landforms*, 5), 956–
1095 977. <https://doi.org/10.1002/esp.4281>, 2018.

1096 Shaller, P. J., Doroudian, M., & Hart, M. W.: The Eureka Valley Landslide: Evidence of a dual failure mechanism for
1097 a Long-Runout Landslide. *Lithosphere*, 2020(1). <https://doi.org/10.2113/2020/8860819>, 2020.

1098 Schürch, P., Densmore, A. L., Rosser, N., & McArdeell, B. W.: Dynamic controls on erosion and deposition on debris-
1099 flow fans. *Geology*, 39(9), 827–830. <https://doi.org/10.1130/g32103.1>, 2011.

1100 Shen, P., Zhang, L. M., Wong, H., Peng, D., Zhou, S., Zhang, S., & Chen, C.: Debris flow enlargement from
1101 entrainment: A case study for comparison of three entrainment models. *Engineering Geology*, 270, 105581.
1102 <https://doi.org/10.1016/j.enggeo.2020.105581>, 2020.

1103 Stock, J. P. J., & Dietrich, W. E.: Erosion of steepland valleys by debris flows. *Geological Society of America Bulletin*,
1104 118(9–10), 1125–1148. <https://doi.org/10.1130/b25902.1>, 2006.

1105 Strauch, R. L., Istanbuluoglu, E., Nudurupati, S. S., Bandaragoda, C., Gasparini, N. M., & Tucker, G. E.: A
1106 hydroclimatological approach to predicting regional landslide probability using Landlab. *Earth Surface Dynamics*,
1107 6(1), 49–75. <https://doi.org/10.5194/esurf-6-49-2018>, 2018.

1108 Takahashi, T.: *Debris Flow* (2nd ed.). CRC Press, Taylor & Francis Group, 2014.

1109 Tucker, G. E., & Bras, R. L.: Hillslope processes, drainage density, and landscape morphology. *Water Resources*
1110 *Research*, 34(10), 2751–2764. <https://doi.org/10.1029/98wr01474>, 1998.

1111 Tucker, G. E., Hancock, G. J.: Modelling landscape evolution. *Earth Surface Processes and Landforms*, 35(1), 28–50.
1112 <https://doi.org/10.1002/esp.1952>, 2010.

1113 Tucker, G. E., McCoy, S., & Hobley, D. E. J.: A lattice grain model of hillslope evolution. *Earth Surface Dynamics*,
1114 6(3), 563–582. <https://doi.org/10.5194/esurf-6-563-2018>, 2018.

1115 Western Regional Climate Center. (n.d.), from <https://wrcc.dri.edu/>, accessed 2017 and 2022

1116 Whipple, K. X., & Dunne, T.: The influence of debris-flow rheology on fan morphology, Owens Valley, California.
1117 *Geological Society of America Bulletin*, 104(7), 887–900. [https://doi.org/10.1130/0016-7606\(1992\)104](https://doi.org/10.1130/0016-7606(1992)104), 1992.

1118 Zhou, G. G. D., Li, S., Song, D., Choi, C. E., & Chen, X.: Depositional mechanisms and morphology of debris flow:
1119 physical modelling. *Landslides*, 16(2), 315–332. <https://doi.org/10.1007/s10346-018-1095-9>, 2019.

1120

1121